

A topological mechanism for robust and efficient global oscillations in biological networks

Chongbin Zheng^{1,2} and Evelyn Tang^{1,2}

¹*Department of Physics and Astronomy, Rice University, Houston, Texas 77005, USA*

²*Center for Theoretical Biological Physics, Rice University, Houston, Texas 77005, USA*

Long and stable timescales are often observed in complex biochemical networks, such as in emergent oscillations. How these robust dynamics persist remains unclear, given the many stochastic reactions and shorter time scales demonstrated by underlying components. We propose a topological model with parsimonious parameters that produces long oscillations around the network boundary, effectively reducing the system dynamics to a lower-dimensional current. Using this to model KaiC, which regulates the circadian rhythm in cyanobacteria, we compare the coherence of oscillations to that in other KaiC models. Our topological model localizes currents on the system edge for an efficient regime with simultaneously increased precision and decreased cost. Further, we introduce a new predictor of coherence from the analysis of spectral gaps, and show that our model saturates a global thermodynamic bound. Our work presents a new mechanism for emergent oscillations in complex biological networks utilizing dissipative cycles to achieve robustness and efficient performance.

I. INTRODUCTION

The reduction of the full system response to a much lower dimensional description has been observed in many complex biological systems, where the system dynamics or behavior reduce to a much smaller phase space [1–3]. However, we still lack good models that can mechanistically account for this dimensionality reduction, or that remain stable under noise or structural heterogeneity. This is exemplified in computational models of memory, that describe specific attractor states which represent persistent memories [4, 5]. However, attractors tend to drift or lose accuracy with noise and it remains an area of open research on how to retain encoded information in these models [4]. Another example is that of long oscillations, such as the circadian rhythm, which are crucial for the regulation of many processes such as metabolism and replication [6, 7]. Previously proposed models such as feedback loops of chemical reactions typically involve either small reaction networks consisting of reactions on a similar timescale as the oscillation itself, or a large number of system-dependent parameters [8–10]. A parsimonious model is still lacking for explaining how such oscillations with their long timescales can emerge from a large phase space of faster chemical reactions. Understanding the principles that govern emergent oscillations is crucial as disruptions in biological clocks lead to decreased health and reproductive fitness in multiple organisms [7, 11–14].

As biological networks including those mentioned above typically have a large phase space of possible reactions, this renders unfeasible exhaustive searches using other approaches like experiments or numerical simulation [15], underscoring the need for simple conceptual methods to provide insight [16–18]. The development of rigorous theory would also shed light on simple design principles for targeted dynamics in synthetic biological systems [19, 20] or in the engineering of reconfigurable

materials, e.g., through dissipative self-assembly [21, 22]. Yet, biology presents challenges for the development of suitable theory due to being stochastic, heterogeneous, and strongly non-equilibrium [15, 23–25]. Hence, the few successful models that exist in biology are often heavily dependent on specific system parameters.

Towards addressing these questions, we propose a mechanism for the dimensional reduction of phase space to robust attractors and long oscillations. In particular, we examine the strongly non-equilibrium feature of a topological model that consists of interlinked “futile cycles”, common non-equilibrium motifs that are so named due to their consumption of ATP only to repeat the same states in the cycle [26, 27]. Yet, these motifs are pervasive in many different biological systems from metabolism to sensory systems, muscular contraction, and protein synthesis. Here, we show that such non-equilibrium motifs can link in a topological manner to support emergent global dynamics that move in a directed fashion around the network boundary. We expand on the topological model first proposed in [29] and apply it to the KaiABC system, which regulates the circadian rhythm of cyanobacteria [30]. The localized edge currents naturally reproduce the kinetic ordering of KaiC phosphorylation cycles [31, 32]. Our work is the first in the literature that connects topological models to a concrete biological system. It also features few parameters compared to alternative models of KaiABC [9, 10] while displaying higher oscillation coherence.

Such striking dynamics on the system boundary are a feature of topological invariants, which in the last few decades have proved useful for analyzing emergent function [33–36]. In stochastic systems, these invariants describe whether distinct chemical or mechanical configurations have a global pattern of transition rates between them that supports edge states [29]. Edge states reduce the system response to a lower dimensional space and offer a mechanism for the emergence of global cycles within a large space of reactions. Powerfully, this response is in-

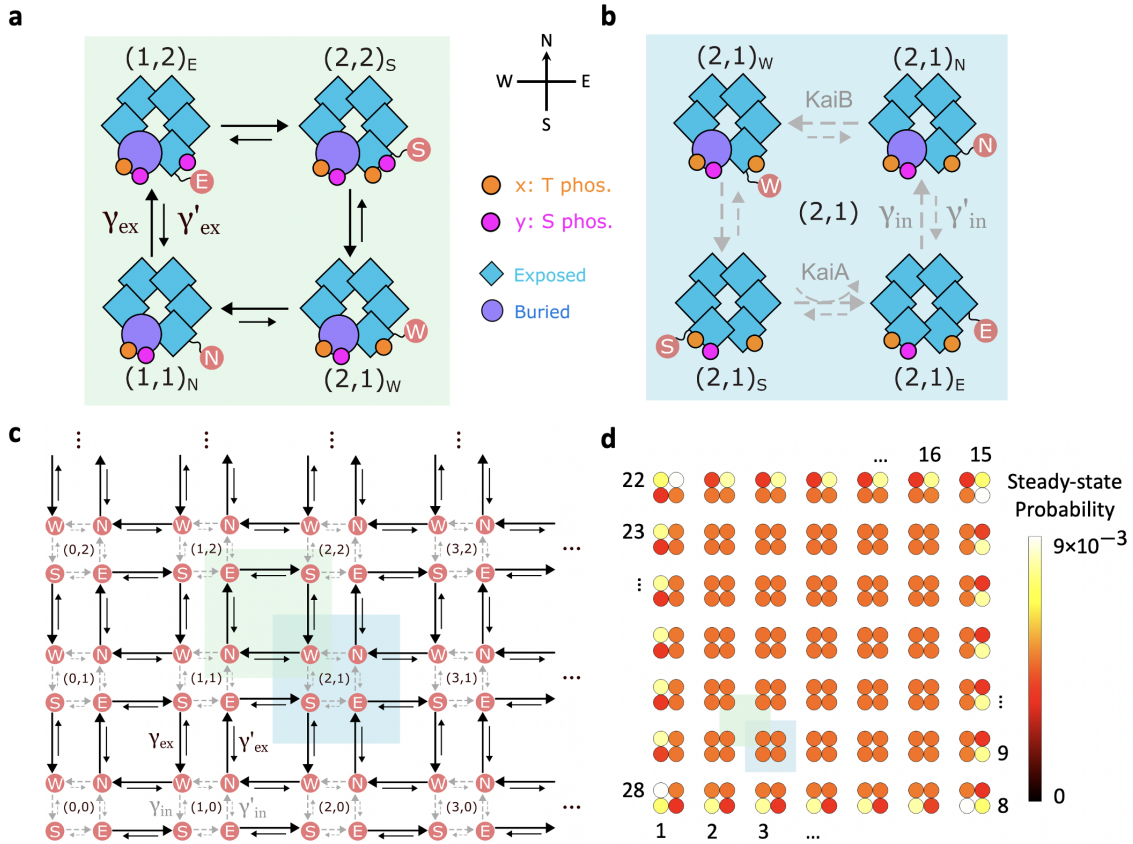


FIG. 1. Topological model for emergent oscillations, illustrated with KaiABC that regulates the circadian rhythm. **a**, Based on the prevalence of non-equilibrium cycles observed in various biological systems [26, 27], we hypothesize that KaiC monomers undergo phosphorylation and dephosphorylation cycles (black arrows γ_{ex} and slower reverse transitions γ'_{ex} , where two types of phosphorylation T and S are shown with the addition of orange and pink circles and the numbers of each are given in brackets). We only keep track of the total phosphorylation levels in T and S, while the location of each phosphorylated monomer can be arbitrary. **b**, Within a given phosphorylation level, internal transitions (grey arrows, γ_{in} and γ'_{in}) can take place due to conformational changes (illustrated by circle and square shapes) or ligand binding (e.g., of KaiA or KaiB). The internal state labels the direction of the next external transition that it primes. We represent the interaction with KaiA with a curly arrow because KaiA promotes phosphorylation by rapid association and dissociation rather than binding to fixed KaiC hexamers [28]. In both **a** and **b**, the curly line from the internal label attaches to the monomer most likely to be modified next, indicating that the monomer is tagged by molecular modifications (e.g. KaiA or KaiB binding) and primed for subsequent change. **c**, These cycles can be laid out in a lattice, with T phosphorylation along the horizontal axis and S phosphorylation along the vertical axis, while each set of four internal transitions (e.g., in the blue box corresponding to **b**) repeats along these axes. The external cycle in **a** is also highlighted in the green box. **d**, This lattice allows probing of its topological properties. In the ordinary case with similar rates throughout, i.e. $\gamma_{ex} \sim \gamma_{in}$, the system will perform a random walk ergodically through the phase space. In the topological regime when $\gamma_{ex} \gg \gamma_{in}$, once the system hits an edge it will continue around the edge, as can be verified by inspection. We plot the steady state in the topological regime which lies on the system edge, taking $\mu = 1, \rho = 2, \gamma_{tot} = 1$. There are 28 states along the edge with high probability, labeled by the order in which they are traversed in a typical trajectory. These trajectories form a global current along the edge of the state space.

sensitive to various types of disorder or noise. These theories could shed light on the fundamental question of why biological function is so robust, e.g., maintaining stable dynamics over long times even in the presence of stochasticity or changing external stimuli. While topological invariants have been heavily studied in quantum electronic systems and observed in other classical platforms such as mechanical lattices [37, 38], they have not yet been identified in biological systems. In this paper, we provide an explicit topological invariant for our model, and demon-

strate the robustness of the emerging oscillations with changing transition rates. We also introduce new methods inspired by topological band theory to characterize oscillation coherence.

The characteristic behavior of our topological model leads to several experimentally testable predictions. For instance, the localization of system dynamics on the edge leads to a novel regime with increasing coherence alongside decreasing energy dissipation as the external driving is increased. This unusual behavior, i.e., “getting more

from pushing less”, has been observed in other scenarios such as driven electronic, Brownian, and glassy systems [39–42], while its occurrence in a stochastic system like ours remains surprising. In this regime, we expect a decrease in total ATP consumption (energy dissipation) in response to an increasing ATP concentration (external driving), a unique signature of our model. Additional experimental predictions are discussed later in the paper, which provide further tests for whether topology as illustrated in our model contributes to the robustness of circadian oscillations.

Interestingly, our approach suggests an alternative mechanism for oscillations from what is typically assumed in the field, such as the Monod-Wyman-Changeux (MWC) paradigm [43]. This paradigm assumes cooperative all-or-none conformational changes for protomers in an oligomer upon ligand binding, which acts as a molecular switch that changes the affinity of all binding sites. The model has been useful in describing systems such as hemoglobin [43], ligand-gated ion channels [44], and bacterial chemotaxis [45]. Still, it remains unclear if the MWC model is the dominant mechanism for other systems. Indeed, models for KaiABC typically assume highly cooperative conformational changes for KaiC monomers in order to obtain oscillations [9, 10, 46, 47]. However, new structural studies suggest that the positive cooperativity between monomer conformational states is fairly weak [48]. Hence, it is timely to examine alternative models that can generate emergent oscillations for macromolecules in the presence of strong internal fluctuations or weak positive cooperativity. Towards this goal, our work proposes a new pathway for the emergence of high coherence despite stochasticity and individual monomer fluctuations, providing a different mechanism to obtain the advantages typically viewed as stemming from strong cooperativity.

II. TOPOLOGICAL MODEL FOR EMERGENT OSCILLATIONS

We consider discrete stochastic processes that operate in a two-dimensional configuration space. The state of the system is completely specified by three variables $(x, y)_s$. The “external” variables x and y are independent dynamical variables. Based on the widespread presence of non-equilibrium cycles in biological systems [26, 27], we propose that the “external” transitions modifying these variables form reaction cycles with transition rates γ_{ex} and slower reverse rates $\gamma'_{ex} \ll \gamma_{ex}$ (black solid arrows), as shown in Fig. 1a. For the KaiABC system, x and y correspond to the number of phosphorylated T and S sites, two residues that can independently phosphorylate on each monomer of the hexameric KaiC molecule [49, 50]. Phosphorylation of these two sites are represented by orange and pink circles in Fig. 1, respectively. In our model, we only keep track of the number of T and S phosphorylated monomers, while the specific location

of each monomer does not matter.

The “internal” variable s , given by compass directions N-E-S-W, labels the internal state of the system that primes it to go through one of the four possible external transitions next. For example, in the W state, the system is most likely to go through the westward external transition that decrements x . Within each phosphorylation level (x, y) , the system can take any of the four possible internal states N, E, S or W that prime each possible external transition. As shown in Fig. 1b, these internal states are also assumed to transition between each other in a cyclic manner, with internal transition rates γ_{in} and slower reverse rates $\gamma'_{in} \ll \gamma_{in}$ (gray dashed arrows). Unlike the external cycles above, the internal cycles typically do not correspond to reaction cycles in biological systems. For the KaiABC system, the internal transitions could correspond to interactions with KaiA and KaiB proteins [51] and conformational changes of a loop-like structure on KaiC called the A-loop (two conformations represented by blue squares and purple circles in Fig. 1 respectively) [52]. These transitions modify the internal state of the system, changing its tendency to phosphorylate or dephosphorylate and whether in T or S. In particular, we assume that the monomer conformational changes occur after S-site phosphorylation of the same monomer. It follows that the states $(x, y)_E$ and $(x, y)_S$ (for $y > 0$) in our model have $y - 1$ circles and $7 - y$ squares, while the states $(x, y)_W$ and $(x, y)_N$ have y circles and $6 - y$ squares. We represent the internal transition associated with KaiA with a curly arrow, since KaiA promotes phosphorylation through rapid association and dissociation, activating a larger stoichiometric amount of KaiC as compared to the typical one-on-one binding like KaiB [28].

These reactions are repeated for each monomer and hence can be laid out as a lattice. As shown in Fig. 1c, the phosphorylation/dephosphorylation cycles in Fig. 1a (green box) and the internal cycles in Fig. 1b (blue box) both repeat along the x and y axes of T and S phosphorylation. Such a lattice will have edges representing the physical constraints of the system, i.e., $0 \leq x \leq N_x$ and $0 \leq y \leq N_y$. In our case, $N_x = N_y = 6$ since there are 6 sites available on a KaiC hexamer for either T or S phosphorylation.

Our model in Fig. 1c is mathematically equivalent to the model introduced in [29], both featuring a lattice structure in a 2D state space. However, when applying to the KaiABC system, the state space of the model in [29] has been re-interpreted towards a more realistic description. In turn, some chemical reactions are no longer present while others have been noted. Specifically, in [29] the external variables x and y represent the number of phosphorylated KaiC monomers and the number of monomer conformational changes, while in our paper these variables are interpreted as the number of T and S phosphorylated monomers. Rather than occurring independently, the conformational change is instead hypothesized to change the system internal state and prime

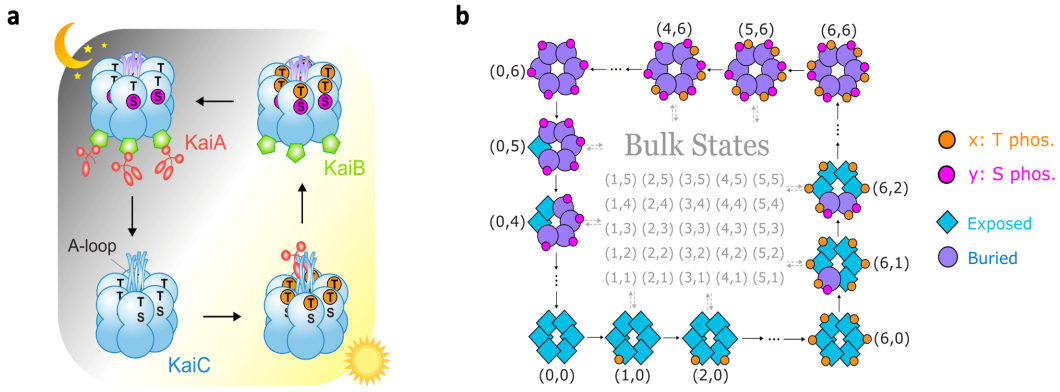


FIG. 2. Phosphorylation cycle of the KaiABC system, reproduced by the topological model. **a**, KaiABC exhibits oscillations via a concerted global cycle of phosphorylation and dephosphorylation. During the day, all six KaiC monomers get phosphorylated at the T-sites, and then at the S-sites. This phosphorylation phase is promoted by interaction with KaiA molecules [53]. By night, fully phosphorylated KaiC binds to KaiB, which sequesters KaiA from the solution. In the absence of KaiA, all the T-sites get dephosphorylated, followed by the S-sites [31]. The A-loop tends to bind KaiA in the exposed state and not bind with KaiA in the buried state [52]. Since individual monomers can independently phosphorylate and shuffle between hexamers [28, 54], why do they perform a concerted phosphorylation cycle that is robust? **b**, In the topological regime, a global cycle emerges similar to the experimentally observed phosphorylation sequence. Here we only show one representative state (out of four) for each phosphorylation level (x, y) along the edge.

subsequent phosphorylations. This is consistent, for example, with studies on A-loop conformational changes on KaiC monomers [52, 55]. We also include interactions with KaiA and KaiB molecules as possible biological reactions that change the internal state of the model.

Before analyzing the model, we simplify our parametrization for the four transition rates γ_{ex} , γ'_{ex} , γ_{in} , γ'_{in} down to three parameters. First, μ is the thermodynamic force defined by $e^{\mu/k_B T} \equiv \gamma_{ex}/\gamma'_{ex} = \gamma_{in}/\gamma'_{in}$. For an arbitrary cycle in the network, the sum of μ along each transition in the cycle is the energy input into that cycle from external driving such as ATP hydrolysis [56]. Detailed balance occurs at $\mu = 0$ while out-of-equilibrium is when $\mu > 0$; we analyze μ in units of $k_B T$. Here we assume the same μ for every transition in the model, which removes one free parameter. Second, ρ varies the ratio of external to internal transitions, defined by $e^\rho \equiv \gamma_{ex}/\gamma_{in} = \gamma'_{ex}/\gamma'_{in}$. It quantifies the separation of timescales between the external and internal transitions. Third, γ_{tot} controls the overall timescale of all transitions, i.e., $\gamma_{tot} \equiv \gamma_{ex} + \gamma'_{ex} + \gamma_{in} + \gamma'_{in}$.

There are two dynamical regimes for the system, determined by tuning the parameter ρ . In the trivial regime when $\rho < 0$, the system tends to go through local counterclockwise cycles via internal transitions γ_{in} , interspersed with slower external transitions γ_{ex} that break out of these cycles. Such behavior is observed both in the bulk and on the edge of the state space. Over long times, the system displays diffusive dynamics and will ergodically explore the whole state space. On the other hand, in the topological regime when $\rho > 0$, the system supports an edge state [29]. In the bulk of the state space, the system would similarly go through local clockwise cycles via external transitions γ_{ex} , interspersed with internal

transitions γ_{in} which are now slower. However, once the system reaches the edge, it will continue around the edge, which can be verified by inspection in Fig. 1c (also see Supplementary Movie). At long times, the steady-state distribution will hence lie on the system edge, forming a global current that flows counterclockwise along the boundary of the lattice; see Fig. 1d. The edge state and the associated dynamical regime have a topological origin, as their emergence is governed by the presence of a topological invariant, the 2D Zak phase [29, 57]. For our topological model, the 2D Zak phase takes the trivial value $(0, 0)$ when $\rho < 0$ but becomes (π, π) in the topological regime $\rho > 0$ (see Supplementary Information for more details). As ρ becomes larger in the topological regime, the Zak phase (π, π) is preserved, while the edge state becomes more localized on the system boundary [58]. The edge state further inherits the useful property of topological protection from inaccessible states [29] or perturbations in transition rates (see Supplementary Fig. S1 and S2). Because of these unusual properties, we focus on the topological regime and investigate the properties of our system assuming $\rho > 0$ from now on.

Experimentally, it is well established that KaiC molecules exhibits 24-hour cycles via a concerted phosphorylation sequence in the presence of KaiA and KaiB [59]. As illustrated in Fig. 2a, during the day, all six KaiC monomers get phosphorylated at the T-sites, and then at the S-sites. By night, all the T-sites get dephosphorylated, again followed by the S-sites [32]. The phosphorylation phase in the day is facilitated by interaction with KaiA [53], while the dephosphorylation phase at night is promoted by binding to KaiB [60]. The robustness of this concerted phosphorylation sequence is surprising, given the large phase space of possible reactions.

For instance, it is known that the monomers can assemble into hexamers and disassemble stochastically, and exhibit directed autophosphorylation-dephosphorylation cycles [54]. Monomers also shuffle between different hexamers [28] and display different conformations within the same hexamer [48]. Given this very large phase space of possible reactions available to individual monomers, why would all the monomers phosphorylate together in a concerted global cycle? Further, since phosphorylation in both T and S are promoted during the day, why does phosphorylation proceed in the specific order where all six T sites get phosphorylated before S phosphorylation begins (Fig. 2a)? To answer this question, models [9, 10, 46, 47] have typically relied on the concerted or Monod-Wyman-Changeux paradigm [43] of allosteric regulation, which restricts the configuration space such that either all or none of the monomers in a complex undergo a conformational change. However, recent cryo-EM data shows that monomers can demonstrate independent conformational changes in the same hexamer [48], challenging this strong restriction. Further, these models often put in by hand the specific ordering of T-site phosphorylation occurring before S-site phosphorylation.

Our topological model presents an alternative way to account for the experimental facts and explain the emergence of the KaiC phosphorylation cycle. Based on experimental evidence for KaiC monomer autophosphorylation [28, 54], we hypothesize directed monomer reaction cycles of phosphorylation and dephosphorylation as illustrated in Fig. 1a. We also propose directed cycles of internal transitions as in Fig. 1b based on experimental results relating A-loop conformations with KaiA and KaiB. For example, A-loop exposure promotes KaiA binding [52] and prohibits KaiB binding [61] while A-loop burial prohibits KaiA binding and promotes KaiB binding [61]. In addition, our hypothesis that KaiA and KaiB preferentially interact with different phosphorylation configurations is consistent with experimental evidence that activation by KaiA is incompatible with the configuration of KaiC that triggers KaiB binding [28]. In particular, we propose that KaiA preferentially interacts with KaiC during T-site phosphorylation rather than S-site phosphorylation, and the converse for KaiB, which agrees with observed data [51]. Indeed, experiments indicate that KaiB binding (and possibly its unbinding), with rates γ_{in} in our model, are slow processes [28, 31, 62, 63] compared to phosphorylation reactions (with rates γ_{ex} in our model) [10] – consistent with our assumption that there is a separation of timescales.

As discussed above, in the topological regime where $\rho \gg 0$, the system supports a propagating edge current. Fig. 2b shows a coarse-grained picture of this edge current, where one of the four internal states is shown for each phosphorylation level (x, y) along the edge, specifically the last state along the edge (e.g. E states for the bottom edge or S states for the left edge). As we can see, the edge current is equivalent to a global cycle of concerted phosphorylation of the T-sites, followed by the

S-sites, then dephosphorylation of the T-sites and, lastly, of the S-sites (also see Supplementary Movie). This provides a mechanism that allows for individual monomers to undergo conformational and other changes, while still producing a global cycle and the experimentally observed phosphorylation sequence that emerges with less fine-tuning.

III. MODEL THERMODYNAMICS: PRECISION VS COST

While this topological model provides an unique alternative mechanism to experimentally observed oscillatory dynamics, how precise or efficient are the oscillations produced? In this section, we quantify the thermodynamics and entropy production of this model, and compare its performance to that of other KaiC models [64–66]. Further, we identify a new predictor for oscillator coherence and analyze the saturation of thermodynamic bounds for different models. We begin by analyzing the master equation that describes stochastic systems,

$$\frac{d\mathbf{p}}{dt} = \mathcal{W}\mathbf{p}, \quad (1)$$

where $\mathbf{p}(t)$ is a vector that describes the probability distribution of system states. \mathcal{W} is the transition matrix, whose elements \mathcal{W}_{ij} specify the transition rates from state j to i . The dynamics of oscillations is typically dominated by the first non-zero eigenvalue of \mathcal{W} , which is the eigenvalue with the smallest modulus in the real part [64], denoted as $-\lambda_R \pm i\lambda_I$ for the real and imaginary parts λ_R and λ_I , respectively. Here $\lambda_R, \lambda_I \geq 0$ and we take $\lambda_1 = -\lambda_R + i\lambda_I$. In general, $\mathbf{p}(t)$ relaxes to the steady-state distribution through damped oscillations, with a decay time λ_R^{-1} and oscillation period $\mathcal{T} = 2\pi/\lambda_I$ [64] (also see Supplementary Fig. S3). Following [64], we define coherence as the ratio

$$\mathcal{R} \equiv \frac{\lambda_I}{\lambda_R}, \quad (2)$$

which quantifies the robustness of sustained oscillations before stochastic noise destroys the coherence (more details in Supplementary Information). We would like to see how our model performs using this metric and what factors contribute to increased coherence.

In typical oscillator models, coherence can be increased by dissipating more free energy. For a general oscillator model described by a master equation, the free energy cost for maintaining the non-equilibrium steady state under constant temperature can be quantified by the entropy production per period ΔS . Denoting the steady-state probability distribution as \mathbf{p}^s and the oscillation period as \mathcal{T} , ΔS is given by [68, 69]

$$\Delta S = \frac{\mathcal{T}}{2} \sum_{i,j} (p_j^s \mathcal{W}_{ij} - p_i^s \mathcal{W}_{ji}) \ln \left(\frac{p_j^s \mathcal{W}_{ij}}{p_i^s \mathcal{W}_{ji}} \right). \quad (3)$$

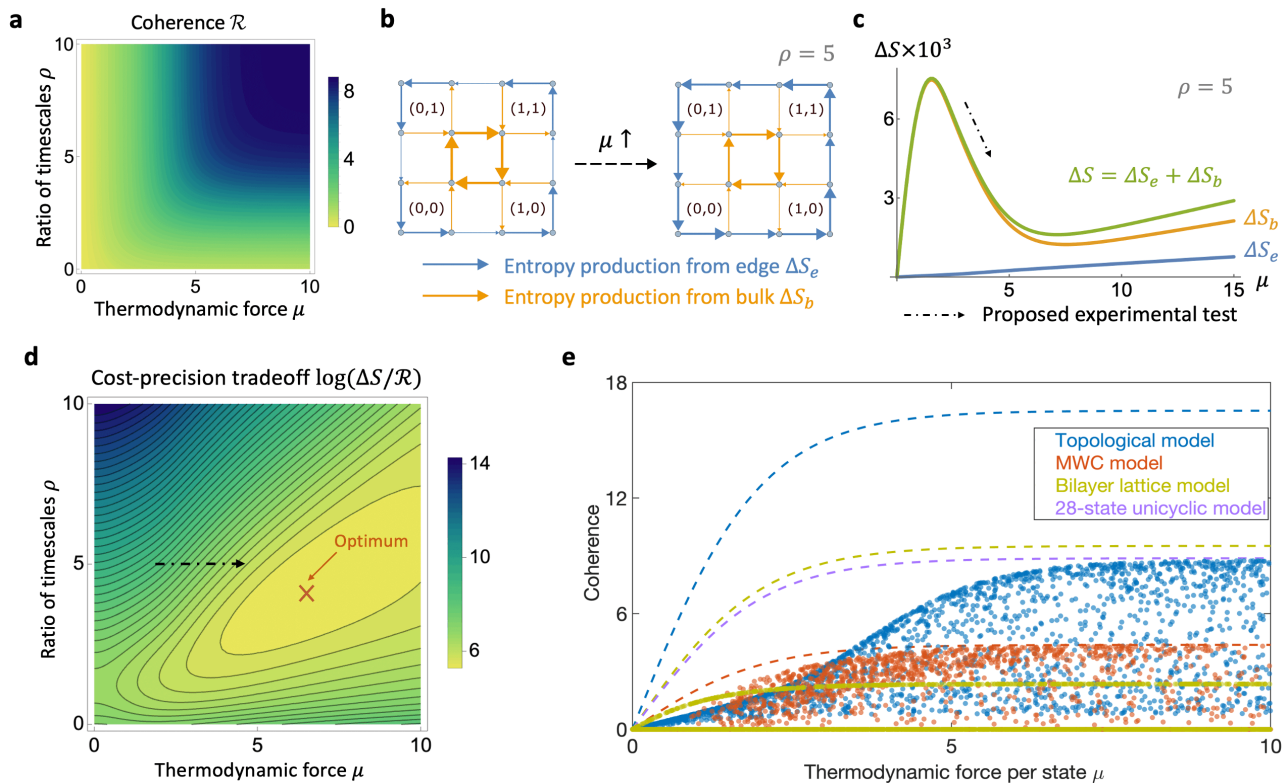


FIG. 3. **Coherence and an efficient regime with simultaneously increased precision and decreased cost.** **a**, Phase diagram of coherence \mathcal{R} for the topological model, which increases with respect to thermodynamic force μ and ratio of timescales ρ as expected. **b**, Entropy production ΔS moves from the bulk to the boundary of the system with increasing μ , illustrated on a smaller lattice. The system is in the topological regime; $\rho = 5$. Blue arrows represent entropy production on the edge ΔS_e and orange arrows represent entropy production in the bulk ΔS_b . Arrow thickness corresponds to the magnitude of the entropy production for the corresponding transitions and arrows point in the direction of the probability flux. **c**, Entropy production per period ΔS for the topological model ($N_x = N_y = 6$) is decomposed into a bulk and an edge contribution. Due to the localization effects in Fig. 3b, the entropy production on the edge ΔS_e (blue) increases while entropy production in the bulk ΔS_b (orange) decreases with μ around $1.5 < \mu < 7$. Typically, the bulk contribution dominates the edge contribution, hence their sum ΔS (green) also decreases with increasing μ . Experimentally, the negative slope in this regime predicts a decreased overall ATP consumption when ATP concentration is increased, as indicated by the black dash-dotted arrow. **d**, Phase diagram of the cost-precision tradeoff $\Delta S/\mathcal{R}$ [67]. The black dash-dotted arrow, similar to that in **c**, indicates increasing μ in the energy-efficient regime. This leads to a lower $\Delta S/\mathcal{R}$, which implies a more cost-effective oscillator. There is a global optimum for $\Delta S/\mathcal{R}$ at $\mu = 6.5, \rho = 4.1$. **e**, Comparison of coherence for different KaiC models with randomly sampled parameters (individual points): there is a strongly-driven regime where the topological model has the highest coherence. The dashed lines represent the upper bounds on coherence for the corresponding models in terms of the thermodynamic force μ [64] (see Methods). The purple dashed line is the upper bound for the 28-state unicyclic model, which is approached by the edge state in the strongly topological regime. Values of ΔS in all panels are given in units of $\gamma_{tot} k_B$.

In the MWC-type model of KaiC studied in [64], for example, increasing ΔS is necessary to increase coherence. Both quantities increase when the external driving μ is stronger, although coherence starts to decrease when μ is increased still further (see Supplementary Fig. S6). This leads to even worse performance for the oscillator as it maintains less coherent oscillations with increasing energetic cost.

On the contrary, our model in the topological regime displays an unusual regime where coherence increases while entropy production per period becomes lower. Fig. 3a shows the coherence of our model as a function of the two parameters μ and ρ (also see Supplementary Fig.

S4 featuring both positive and negative ρ). Increasing the thermodynamic force increases coherence monotonically, as expected for typical oscillator models [64]. Going deeper into the topological regime by increasing ρ also leads to higher coherence, as the global currents become more localized on the system edge [58]. However, the entropy production per period ΔS does not change monotonically with μ . As illustrated in Fig. 3b in a smaller lattice, the system response becomes localized to the edge as μ increases. This causes the entropy production on the edge (blue arrows) to increase, while the entropy production in the bulk (orange arrows) decreases, in the region $1.5 < \mu < 7$. Since the bulk contribution typically domi-

nates the edge contribution, i.e., $\mathcal{O}(N^2) \gg \mathcal{O}(N)$ where N is the typical system size, the sum of their contributions also decreases (green curve in Fig. 3c). This negative slope of ΔS with respect to μ implies that the system dissipates less free energy overall even when the external driving μ supplied to each reaction is stronger. In other words, we “get more from pushing less” [39–42]. This unusual regime has a topological origin, since the decrease in the bulk entropy production results from the localization of the steady state onto the system edge. This unusual negative slope leads to a unique experimental signature. Where ΔS has a negative slope, increasing the ATP concentration (increasing μ) leads to a decrease in total ATP consumption (decreasing ΔS). This is a striking prediction of our topological model, as shown by the dash-dotted arrow in Fig. 3c. In addition, since coherence increases monotonically with μ , this leads to an efficient regime with simultaneously increasing coherence and decreasing cost. The cost-effectiveness in terms of expending free energy for coherent oscillations can be measured by the ratio $\Delta S/\mathcal{R}$ [67]. See Fig. 3d for the region in parameter space with low $\Delta S/\mathcal{R}$, indicating a highly efficient oscillator.

We can further compare coherence between different families of KaiC models. We include a simple MWC-type model [64] and a bilayer model that has a lattice structure more similar to ours, adapted from Li et al. [66] (details of each in Supplementary Information). Each layer in the bilayer lattice represents the T and S phosphorylation levels along its x and y coordinates similar to our topological model, with the possibility to switch between the two layers that denote unbound KaiC and KaiB-bound KaiC, respectively (See Supplementary Fig. S5b and S5c). KaiC is more likely to bind to KaiB on the upper right half of each lattice and more likely to unbind on the lower left half. In order to aid comparison, we simplify this lattice model using our (μ, ρ) parameters (details in Supplementary Information).

By sampling random parameters in the three models, we find a regime of high thermodynamic driving where the topological model has the highest coherence (Fig. 3e). In the same plot, we also indicate a thermodynamic bound for coherence [64] for each model (dashed lines), which depend on the system size and thermodynamic force μ (see Methods). We also plot the bound for a 28-state unicyclic model (purple dashed line in Fig. 3e), which our model approaches in the limit of high μ and high ρ . This is because there are 28 slow internal transitions on the edge that form the effective bottleneck and dominate over the other fast external transitions, resulting in 28 high-probability states as noted in Fig. 1d. This shows that our topological model approaches the bound set by the most coherent cycle, which is the unicycle with uniform rates (γ_{in} and γ'_{in} in our case) [64], deep in the topological regime with high external driving.

Given the high coherence of our model, we would like to identify the factors that determine high coherence. Here, we introduce a new predictor of coherence, which is the

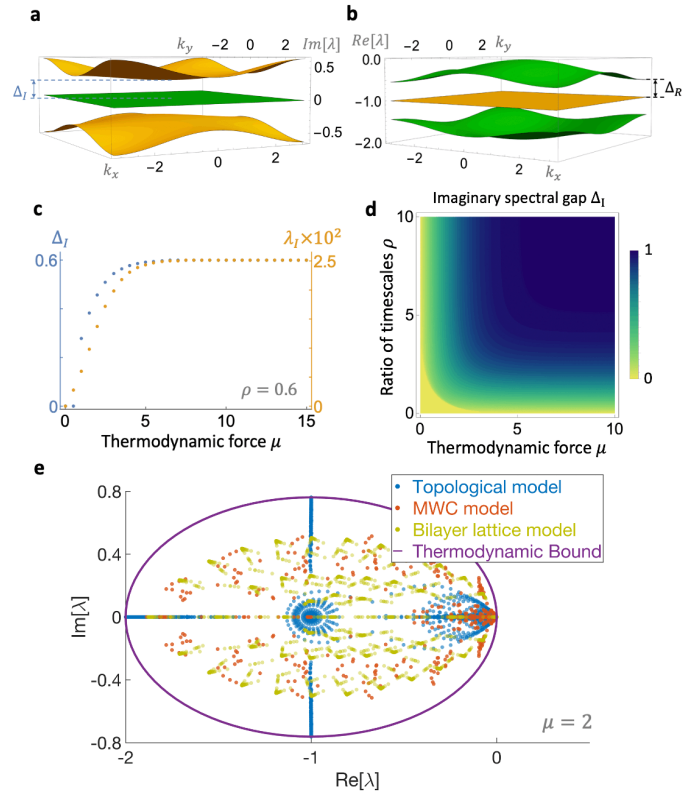


FIG. 4. New predictor of coherence and saturation of a global thermodynamic bound. **a,b**, Spectrum for the topological model in reciprocal space in imaginary space (**a**) and real space (**b**) for $\mu = 1.5$ and $\rho = 1$. The spectral gaps Δ_I and Δ_R are defined as the difference between the minimum of the topmost band and the maximum of the second band. **c**, The imaginary spectral gap Δ_I closely tracks the imaginary part λ_I of the first non-zero eigenvalue λ_1 , as a function of μ . **d**, Phase diagram for the imaginary spectral gap Δ_I in μ and ρ . Δ_I and coherence (Fig. 3a) track each other monotonically, and both saturate to a maximum value after a rapid increase. **e**, The global spectral bound for a fixed μ is shown by a purple ellipse in the complex plane [70], while points represent the spectra for the transition matrix \mathcal{W} for different oscillator models. The topological model approaches this bound in the limit $\rho \rightarrow \infty$, which is saturated by the most coherent cycle (the unicycle) [70]. Here $\mu = 2$ and other parameters are randomly sampled. In all panels, eigenvalues are given in units of γ_{tot} .

spectral gap (or band gap) of the system, inspired from band theory of solids [71]. As the spectral gap measures the separation between modes with different timescales [68], a larger gap predicts greater separation between modes and hence the stability of longer-lived modes as they mix less with transient ones. See Fig. 4a and 4b for the spectral gap in both imaginary and real space, Δ_I and Δ_R respectively, in the reciprocal space version of our topological model (see Supplementary Information for more details). The spectral gap is defined as the difference between the minimum of the topmost band and the maximum of the band below it. Comparing Δ_I with

the imaginary part λ_I of the first non-zero eigenvalue λ_1 in Fig. 4c, we see that they track each other well as μ is increased. Since coherence \mathcal{R} is the ratio of λ_I to its corresponding real part λ_R of the same eigenvalue (Eq. 2) and λ_R remains roughly constant with increasing μ (see Supplementary Fig. S8), Δ_I tracks \mathcal{R} (Fig. 3a) monotonically in μ as well. Along the other axis, increasing ρ decreases the spectral dispersion, i.e. it compresses the top band in Fig. 4a. The topmost point of the top band also increases with ρ while the middle green bands in Fig. 4a remain flat, leading to a widened spectral gap Δ_I for increasing ρ . Moreover, λ_R decreases more quickly than λ_I with increasing ρ , so that their ratio \mathcal{R} increases (see Supplementary Fig. S8). Therefore, Δ_I tracks coherence in ρ as well. Hence, both the imaginary spectral gap and coherence track each other monotonically, as can be seen in their phase diagrams Figs. 4d and 3a respectively, where both saturate to a maximum following a rapid increase.

Lastly, we examine how the different models perform compared to a conjectured global thermodynamic bound on the full spectrum of \mathcal{W} [70]. For a given thermodynamic force, the spectrum is found to lie within an ellipse in the complex plane (purple line in Fig. 4e). The most coherent cycle, a unicyclic network with uniform rates [64], saturates this bound [70]. While the other two families of KaiC models do not saturate the bound for any sampled parameters, our model approaches this bound as $\rho \rightarrow \infty$. This is consistent with our model approaching a uniform unicyclic network when ρ is large, and also with our previous analysis of the spectral gap contributing to high coherence. Similar to the results in reciprocal space model discussed above, the transition matrix \mathcal{W} also shows a larger imaginary spectral gap as ρ increases, which moves the topmost eigenvalue upward in the complex plane and saturates the global spectral bound while increasing coherence (see Supplementary Information and Fig. S7 for details).

IV. DISCUSSION

We have proposed a topological model that generates coherent oscillations, which supports an unusual regime with increased coherence and simultaneously decreased energetic cost. The mathematical model, which first appeared in [29], is interpreted in a biological context and applied to the KaiABC system. Compared to other KaiABC models, our model has high coherence and more closely saturates a global spectral bound, similar to the most coherent unicyclic models. We also find that the imaginary spectral gap can be used to predict oscillation coherence. Further, the kinetic ordering of the KaiABC phosphorylation cycle arises naturally as an edge current in our model. In contrast to typical MWC-type models which usually involve a large number of system-dependent parameters [9, 10], our model is parsimonious in that it captures the same phosphorylation dynamics

with only a few parameters. Moreover, it also does not require fine-tuning of the reaction rates or restriction of the configuration space to all-or-none conformational change, an assumption that is not supported by emerging experimental evidence [48].

We further predict testable signatures of topological edge states in biological oscillators and the KaiABC system. By changing the ATP concentration or ATP/ADP ratio, we can tune the thermodynamic force μ into the regime where ΔS has a negative slope in μ (dash-dotted arrow in Fig. 3c). In this regime, we expect to measure decreased ATP consumption as ATP concentration is increased, a unique feature of our topological model. Moreover, examining our steady-state distribution (Fig. 1d), we expect to find mixtures of molecules with specific fractions of differentially phosphorylated subunits, which may be measured by mass spectrometry [72]. Further, KaiB-bound KaiC should be less abundant than unbound KaiC, because the slow γ_{in} transitions cause a buildup of the latter before they bind to KaiB. Lastly, by perturbing the system or initializing it in the bulk of the state space with partially phosphorylated T and S sites, we should see a transient increase in ATP consumption or energy dissipation as the system goes through rapid cycles of external transitions within the system bulk before converging to the edge. Monomer phosphorylation cycles in the reverse direction from the global cycle may also be observed, as the external cycles in the system bulk have the opposite chirality from our global cycle on the system edge (see Fig. 1c).

Our model gives rise to the observed sequence of phosphorylation reactions in KaiABC without having to tune as many free parameters as in typical models [9, 10]. This is due to the repetition of simple motifs in our network, such that these motifs are governed by only a handful of free parameters. Further, we note that population effects in KaiABC are known to be important, e.g., by promoting the synchronization of many molecules in the KaiABC system [9, 31, 59]. Still, the oscillation and coherence of individual molecules are generally presumed to be building blocks for sustained oscillations at the population level, even while the extent of the single-molecule contribution remains unclear. Hence, our work focuses on the oscillations and coherence of single molecules as a first step towards the understanding of population-level coherence more generally, with the exploration of multiple molecules and their synchronization to be left for future work. See Section VII in Supplementary Information for preliminary work on generalizing our single-molecule model to many molecules and incorporating population-level effects such as competition for KaiA molecules.

By rigorously embedding topological methods within non-equilibrium statistical physics, our work generalizes their usage for various biological and chemical systems. Our results suggest a new mechanism that utilizes dissipative cycles to produce emergent oscillations or attractor states in biological systems. This mechanism can be tested by introducing perturbation or mutant proteins

[73], in order to jointly analyze how these changes modify the robustness and coherence of the global cycle. Even though we have mostly discussed our model in the context of the KaiABC system, the model is more general. It can be mapped to various other biological systems where x and y represent other possible types of molecular modifications such as polymerization [29]. More broadly, our model provides a blueprint for the design for synthetic oscillators, which is becoming increasingly feasible due to new experimental developments [74, 75]. While designing synthetic oscillators that are robust across different parameters or changes in the environment remains a challenge [76, 77], this project provides new models for robust oscillators and continuous attractor dynamics in

various biochemical scenarios and changing conditions.

DATA AVAILABILITY

The data supporting the main findings of this study are available in the paper and its Supplementary Information. Any additional data can be available from the authors upon request.

CODE AVAILABILITY

The code used to generate the data for the figures in our manuscript is available upon request.

-
- [1] M. Rigotti, O. Barak, M. R. Warden, X.-J. Wang, N. D. Daw, E. K. Miller, and S. Fusi, The importance of mixed selectivity in complex cognitive tasks, *Nature* **497**, 585 (2013).
- [2] E. Tang, M. G. Mattar, C. Giusti, D. M. Lydon-Staley, S. L. Thompson-Schill, and D. S. Bassett, Effective learning is accompanied by high-dimensional and efficient representations of neural activity, *Nature neuroscience* **22**, 1000 (2019).
- [3] G. J. Stephens, B. Johnson-Kerner, W. Bialek, and W. S. Ryu, Dimensionality and dynamics in the behavior of *C. elegans*, *PLoS computational biology* **4**, e1000028 (2008).
- [4] R. Chaudhuri and I. Fiete, Computational principles of memory, *Nature neuroscience* **19**, 394 (2016).
- [5] J. J. Hopfield, Neural networks and physical systems with emergent collective computational abilities., *Proceedings of the national academy of sciences* **79**, 2554 (1982).
- [6] Y. Liao and M. J. Rust, The circadian clock ensures successful dna replication in cyanobacteria, *Proceedings of the National Academy of Sciences* **118**, e2022516118 (2021).
- [7] A. M. Puszynska and E. K. O’Shea, Switching of metabolic programs in response to light availability is an essential function of the cyanobacterial circadian output pathway, *elife* **6**, e23210 (2017).
- [8] P. Smolen, D. A. Baxter, and J. H. Byrne, Modeling circadian oscillations with interlocking positive and negative feedback loops, *Journal of Neuroscience* **21**, 6644 (2001).
- [9] J. S. van Zon, D. K. Lubensky, P. R. Altena, and P. R. ten Wolde, An allosteric model of circadian KaiC phosphorylation, *Proceedings of the National Academy of Sciences* **104**, 7420 (2007).
- [10] J. Pajmans, D. K. Lubensky, and P. R. Ten Wolde, A thermodynamically consistent model of the post-translational Kai circadian clock, *PLoS computational biology* **13**, e1005415 (2017).
- [11] R. M. Green, S. Tingay, Z.-Y. Wang, and E. M. Tobin, Circadian rhythms confer a higher level of fitness to Arabidopsis plants, *Plant physiology* **129**, 576 (2002).
- [12] M. Horn, O. Mitesser, T. Hovestadt, T. Yoshii, D. Rieger, and C. Helfrich-Förster, The circadian clock improves fitness in the fruit fly, *Drosophila melanogaster*, *Frontiers in Physiology* **10**, 1374 (2019).
- [13] F. A. Scheer, M. F. Hilton, C. S. Mantzoros, and S. A. Shea, Adverse metabolic and cardiovascular consequences of circadian misalignment, *Proceedings of the National Academy of Sciences* **106**, 4453 (2009).
- [14] S. Masri and P. Sassone-Corsi, The emerging link between cancer, metabolism, and circadian rhythms, *Nature medicine* **24**, 1795 (2018).
- [15] A. L. Dewyer, A. J. Argüelles, and P. M. Zimmerman, *Methods for exploring reaction space in molecular systems*, Wiley Interdisciplinary Reviews: Computational Molecular Science **8**, e1354 (2018).
- [16] P. Davies, Does new physics lurk inside living matter?, *Physics today* **73**, 34 (2020).
- [17] A. T. Winfree, *The geometry of biological time*, Vol. 2 (Springer, 1980).
- [18] P. Gao and S. Ganguli, On simplicity and complexity in the brave new world of large-scale neuroscience, *Current opinion in neurobiology* **32**, 148 (2015).
- [19] J. Doudna, R. Bar-Ziv, J. Elf, V. Noireaux, J. Berro, L. Saiz, D. Vavylonis, J.-L. Faulon, and P. Fordyce, How will kinetics and thermodynamics inform our future efforts to understand and build biological systems?, *Cell Systems* **4**, 144 (2017).
- [20] P. Schwille, J. Spatz, K. Landfester, E. Bodenschatz, S. Herminghaus, V. Sourjik, T. J. Erb, P. Bastiaens, R. Lipowsky, A. Hyman, *et al.*, MaxSynBio: avenues towards creating cells from the bottom up, *Angewandte Chemie International Edition* **57**, 13382 (2018).
- [21] J. Deng and A. Walther, ATP-Responsive and ATP-Fueled Self-Assembling Systems and Materials, *Advanced Materials* **32**, 2002629 (2020).
- [22] B. Rieß, R. K. Grötsch, and J. Boekhoven, The design of dissipative molecular assemblies driven by chemical reaction cycles, *Chem* **6**, 552 (2020).
- [23] J. Ross and A. P. Arkin, Complex systems: from chemistry to systems biology, *Proceedings of the National Academy of Sciences* **106**, 6433 (2009).
- [24] G. Ashkenasy, T. M. Hermans, S. Otto, and A. F. Taylor, *Systems chemistry*, Chemical Society Reviews **46**, 2543 (2017).
- [25] H. Qian and H. Ge, *Stochastic Chemical Reaction Systems in Biology* (Springer, 2021).

- [26] J. J. Hopfield, Kinetic proofreading: a new mechanism for reducing errors in biosynthetic processes requiring high specificity, *Proceedings of the National Academy of Sciences* **71**, 4135 (1974).
- [27] M. Samoilov, S. Plyasunov, and A. P. Arkin, Stochastic amplification and signaling in enzymatic futile cycles through noise-induced bistability with oscillations, *Proceedings of the National Academy of Sciences* **102**, 2310 (2005).
- [28] H. Kageyama, T. Nishiwaki, M. Nakajima, H. Iwasaki, T. Oyama, and T. Kondo, Cyanobacterial circadian pace-maker: Kai protein complex dynamics in the KaiC phosphorylation cycle in vitro, *Molecular cell* **23**, 161 (2006).
- [29] E. Tang, J. Agudo-Canalejo, and R. Golestanian, Topology protects chiral edge currents in stochastic systems, *Physical Review X* **11**, 031015 (2021).
- [30] M. Ishiura, S. Kutsuna, S. Aoki, H. Iwasaki, C. R. Andersson, A. Tanabe, S. S. Golden, C. H. Johnson, and T. Kondo, Expression of a gene cluster kaiABC as a circadian feedback process in cyanobacteria, *Science* **281**, 1519 (1998).
- [31] M. J. Rust, J. S. Markson, W. S. Lane, D. S. Fisher, and E. K. O'Shea, Ordered phosphorylation governs oscillation of a three-protein circadian clock, *Science* **318**, 809 (2007).
- [32] S. E. Cohen and S. S. Golden, Circadian rhythms in cyanobacteria, *Microbiology and Molecular Biology Reviews* **79**, 373 (2015).
- [33] J. E. Moore, The birth of topological insulators, *Nature* **464**, 194 (2010).
- [34] C.-K. Chiu, J. C. Teo, A. P. Schnyder, and S. Ryu, Classification of topological quantum matter with symmetries, *Reviews of Modern Physics* **88**, 035005 (2016).
- [35] H. L. Stormer, D. C. Tsui, and A. C. Gossard, The fractional quantum hall effect, *Reviews of Modern Physics* **71**, S298 (1999).
- [36] E. Tang and X.-G. Wen, Interacting one-dimensional fermionic symmetry-protected topological phases, *Physical Review Letters* **109**, 096403 (2012).
- [37] C. Kane and T. Lubensky, Topological boundary modes in isostatic lattices, *Nature Physics* **10**, 39 (2014).
- [38] R. Süsstrunk and S. D. Huber, Observation of phononic helical edge states in a mechanical topological insulator, *Science* **349**, 47 (2015).
- [39] E. M. Conwell, Negative differential conductivity, *Physics Today* **23**, 35 (1970).
- [40] M. Kostur, L. Machura, P. Hänggi, J. Luczka, and P. Talkner, Forcing inertial brownian motors: Efficiency and negative differential mobility, *Physica A: Statistical Mechanics and its Applications* **371**, 20 (2006).
- [41] R. L. Jack, D. Kelsey, J. P. Garrahan, and D. Chandler, Negative differential mobility of weakly driven particles in models of glass formers, *Physical Review E* **78**, 011506 (2008).
- [42] R. Zia, E. L. Praestgaard, and O. Mouritsen, Getting more from pushing less: Negative specific heat and conductivity in nonequilibrium steady states, *American Journal of Physics* **70**, 384 (2002).
- [43] J. Monod, J. Wyman, and J.-P. Changeux, On the nature of allosteric transitions: a plausible model, *Journal of molecular biology* **12**, 88 (1965).
- [44] N. Calimet, M. Simoes, J.-P. Changeux, M. Karplus, A. Taly, and M. Cecchini, A gating mechanism of pentameric ligand-gated ion channels, *Proceedings of the National Academy of Sciences* **110**, E3987 (2013).
- [45] B. A. Mello and Y. Tu, An allosteric model for heterogeneous receptor complexes: understanding bacterial chemotaxis responses to multiple stimuli, *Proceedings of the National Academy of Sciences* **102**, 17354 (2005).
- [46] Y.-G. Chang, R. Tseng, N.-W. Kuo, and A. LiWang, Rhythmic ring-ring stacking drives the circadian oscillator clockwise, *Proceedings of the National Academy of Sciences* **109**, 16847 (2012).
- [47] D. Zhang, Y. Cao, Q. Ouyang, and Y. Tu, The energy cost and optimal design for synchronization of coupled molecular oscillators, *Nature physics* **16**, 95 (2020).
- [48] X. Han, D. Zhang, L. Hong, D. Yu, Z. Wu, T. Yang, M. Rust, Y. Tu, and Q. Ouyang, Determining subunit-subunit interaction from statistics of cryo-em images: observation of nearest-neighbor coupling in a circadian clock protein complex, *Nature Communications* **14**, 5907 (2023).
- [49] T. Nishiwaki, Y. Satomi, M. Nakajima, C. Lee, R. Kiyohara, H. Kageyama, Y. Kitayama, M. Temamoto, A. Yamaguchi, A. Hijikata, *et al.*, Role of KaiC phosphorylation in the circadian clock system of *Synechococcus elongatus* PCC 7942, *Proceedings of the National Academy of Sciences* **101**, 13927 (2004).
- [50] R. Pattanayek, J. Wang, T. Mori, Y. Xu, C. H. Johnson, and M. Egli, Visualizing a circadian clock protein: crystal structure of KaiC and functional insights, *Molecular cell* **15**, 375 (2004).
- [51] J. Lin, J. Chew, U. Chockanathan, and M. J. Rust, Mixtures of opposing phosphorylations within hexamers precisely time feedback in the cyanobacterial circadian clock, *Proceedings of the National Academy of Sciences* **111**, E3937 (2014).
- [52] Y.-I. Kim, G. Dong, C. W. Carruthers Jr, S. S. Golden, and A. LiWang, The day/night switch in KaiC, a central oscillator component of the circadian clock of cyanobacteria, *Proceedings of the National Academy of Sciences* **105**, 12825 (2008).
- [53] Y. Xu, T. Mori, and C. H. Johnson, Cyanobacterial circadian clockwork: roles of KaiA, KaiB and the kaiBC promoter in regulating KaiC, *The EMBO Journal* **22**, 2117 (2003).
- [54] C. Brettschneider, R. J. Rose, S. Hertel, I. M. Axmann, A. J. Heck, and M. Kollmann, A sequestration feedback determines dynamics and temperature entrainment of the KaiABC circadian clock, *Molecular Systems Biology* **6**, 389 (2010).
- [55] R. Tseng, Y.-G. Chang, I. Bravo, R. Latham, A. Chaudhary, N.-W. Kuo, and A. LiWang, Cooperative KaiA-KaiB-KaiC interactions affect KaiB/SasA competition in the circadian clock of cyanobacteria, *Journal of molecular biology* **426**, 389 (2014).
- [56] T. L. Hill, *Free energy transduction and biochemical cycle kinetics* (Springer-Verlag New York Inc., 1989).
- [57] F. Liu and K. Wakabayashi, Novel topological phase with a zero berry curvature, *Physical review letters* **118**, 076803 (2017).
- [58] A. Nelson and E. Tang, Non-reciprocity permits edge states and strong localization in stochastic topological systems, *arXiv preprint arXiv:2310.16720* (2023).
- [59] M. Nakajima, K. Imai, H. Ito, T. Nishiwaki, Y. Murayama, H. Iwasaki, T. Oyama, and T. Kondo, Reconstitution of circadian oscillation of cyanobacterial KaiC phosphorylation in vitro, *science* **308**, 414 (2005).

- [60] Y. Kitayama, H. Iwasaki, T. Nishiwaki, and T. Kondo, KaiB functions as an attenuator of KaiC phosphorylation in the cyanobacterial circadian clock system, *The EMBO journal* **22**, 2127 (2003).
- [61] Y.-G. Chang, N.-W. Kuo, R. Tseng, and A. LiWang, Flexibility of the C-terminal, or CII, ring of KaiC governs the rhythm of the circadian clock of cyanobacteria, *Proceedings of the National Academy of Sciences* **108**, 14431 (2011).
- [62] J. Abe, T. B. Hiyama, A. Mukaiyama, S. Son, T. Mori, S. Saito, M. Osako, J. Wolanin, E. Yamashita, T. Kondo, *et al.*, Atomic-scale origins of slowness in the cyanobacterial circadian clock, *Science* **349**, 312 (2015).
- [63] D. Simon, A. Mukaiyama, Y. Furuike, and S. Akiyama, Slow and temperature-compensated autonomous disassembly of kaiB–kaiC complex, *Biophysics and Physicobiology* **19**, e190008 (2022).
- [64] A. C. Barato and U. Seifert, Coherence of biochemical oscillations is bounded by driving force and network topology, *Physical Review E* **95**, 062409 (2017).
- [65] R. Marsland III, W. Cui, and J. M. Horowitz, The thermodynamic uncertainty relation in biochemical oscillations, *Journal of the Royal Society Interface* **16**, 20190098 (2019).
- [66] C. Li, X. Chen, P. Wang, and W. Wang, Circadian KaiC phosphorylation: a multi-layer network, *PLoS computational biology* **5**, e1000568 (2009).
- [67] L. Oberreiter, U. Seifert, and A. C. Barato, Universal minimal cost of coherent biochemical oscillations, *Physical Review E* **106**, 014106 (2022).
- [68] J. Schnakenberg, Network theory of microscopic and macroscopic behavior of master equation systems, *Reviews of Modern physics* **48**, 571 (1976).
- [69] H. Ge and H. Qian, Physical origins of entropy production, free energy dissipation, and their mathematical representations, *Physical Review E* **81**, 051133 (2010).
- [70] M. Uhl and U. Seifert, Affinity-dependent bound on the spectrum of stochastic matrices, *Journal of Physics A: Mathematical and Theoretical* **52**, 405002 (2019).
- [71] C. Kittel, *Solid state physics*, Vol. 3 (Shell Development Company, 1955).
- [72] S. Mehmood, T. M. Allison, and C. V. Robinson, Mass spectrometry of protein complexes: from origins to applications, *Annual review of physical chemistry* **66**, 453 (2015).
- [73] A. G. Chavan, J. A. Swan, J. Heisler, C. Sancar, D. C. Ernst, M. Fang, J. G. Palacios, R. K. Spangler, C. R. Bagshaw, S. Tripathi, *et al.*, Reconstitution of an intact clock reveals mechanisms of circadian timekeeping, *Science* **374**, eabd4453 (2021).
- [74] V. Klingel, D. Graf, S. Weirich, A. Jeltsch, and N. E. Radde, Model-based design of a synthetic oscillator based on an epigenetic methylation memory system, *ACS Synthetic Biology* **11**, 2445 (2022).
- [75] A. H. Chen, D. Lubkowitz, V. Yeong, R. L. Chang, and P. A. Silver, Transplantability of a circadian clock to a noncircadian organism, *Science advances* **1**, e1500358 (2015).
- [76] M. L. Woods, M. Leon, R. Perez-Carrasco, and C. P. Barnes, A statistical approach reveals designs for the most robust stochastic gene oscillators, *ACS synthetic biology* **5**, 459 (2016).
- [77] Ž. Pušnik, M. Mraz, N. Zimic, and M. Moškon, Computational analysis of viable parameter regions in models of synthetic biological systems, *Journal of biological engineering* **13**, 1 (2019).
- [78] D. T. Gillespie, Exact stochastic simulation of coupled chemical reactions, *The journal of physical chemistry* **81**, 2340 (1977).

METHODS

Simulation of the system steady-state. The steady-state probability distribution in Fig. 1d is obtained by simulating the system dynamics with the Gillespie algorithm [78]. The simulation is run for 10^8 steps with a random initial condition, and the probability for each state is given by the fraction of time the system spends in that state. By calculating the steady-state probability flux $J_{ij} = p_j^s \mathcal{W}_{ij} - p_i^s \mathcal{W}_{ji}$ from state j to i , we obtain the global counterclockwise current along the edge of the lattice, illustrated with black arrows in Fig. 1d.

Thermodynamic bound for coherence. Ref. [64] conjectures an upper bound for coherence for any stochastic system. Suppose that a cycle κ has N_κ states labeled by $\kappa_1, \kappa_2, \dots, \kappa_{N_\kappa}$ such that κ_1 is connected to κ_{N_κ} and κ_2, κ_2 is connected to κ_1 and κ_3 , etc. Define the affinity of κ as $\mathcal{A}_\kappa \equiv \ln \prod_{i=1}^{N_\kappa} \frac{\mathcal{W}_{\kappa_{i+1}\kappa_i}}{\mathcal{W}_{\kappa_i\kappa_{i+1}}}$, where $\kappa_{N_\kappa+1}$ is the same as κ_1 . For an arbitrary stochastic model, we look at all possible cycles in the underlying network. The upper bound for coherence in Fig. 3e is given by

$$\mathcal{R} \leq \max_{\kappa} \{ \cot(\pi/N_\kappa) \tanh[\mathcal{A}_\kappa/(2N_\kappa)] \}.$$

For the topological model, the thermodynamic force per state $\mathcal{A}_\kappa/N_\kappa$ is always μ , and the cycle that maximizes the right hand side of the bound is the global cycle going around the boundary with $N_\kappa = 52$.

Global spectral bound for a driven stochastic system. The global bound in Fig. 4e is conjectured by [70] for the spectrum of any transition matrix for a master equation. To obtain the bound, we look for a cycle that maximizes the affinity per state $\mathcal{A}_\kappa/N_\kappa$. Denote this

maximum by \mathcal{A}_C/N_C . We also define $w_0 = \max_i [|\mathcal{W}_{ii}|]$. The spectrum is hypothesized to lie entirely in the ellipse given by

$$g(x) = w_0 \{ -1 + \cos(2\pi x) + i \tanh[\mathcal{A}_C/(2N_C)] \sin(2\pi x) \}.$$

For the topological model, we have $\mathcal{A}_C/N_C = \mu$. The bound for $\mu = 2$ is plotted in purple in Fig. 4e. Each model has a different w_0 for their corresponding transition matrix. To plot all spectra under a common bound, we rescale each transition matrix by a constant factor such that $w_0 = 1$ for all transition matrices considered.

Sampling random parameters In Fig. 3e, for the topological model and the bilayer lattice model, we randomly select the parameters $\mu \in [0, 10]$ and $\rho \in [0, 7]$ from uniform distributions on each interval. For the MWC model in [64] (see Supplementary Information for parameter definitions), we select from the uniform distributions $\gamma \in [3, 7]$, $E \in [5, 15]$ and $\eta \in [0, \frac{70}{3}]$. The parametrization of the MWC model is such that the maximum affinity per state is $\mathcal{A}/N = \frac{3}{7}\eta$. Because we keep \mathcal{A}/N (which we also call thermodynamic force per state and simply denote as μ) the same in Fig. 3e, $\eta \in [0, \frac{70}{3}]$ exactly corresponds to $\mu \in [0, 10]$. For Fig. 4e, we fix the thermodynamic force per state $\mu = 2$ (which is $\eta = \frac{14}{3}$ for the MWC model) and sample the remaining parameters ρ , γ , and E in the same way as above.

ACKNOWLEDGEMENT

We are grateful to Jordan Horowitz, David Lubensky, Jaime Agudo-Canalejo, Yuhai Tu and Michael Rust for helpful discussions. In addition, we thank Pankaj Mehta, Peter Wolynes, Ulrich Schwarz and Oleg Igoshin for their thoughtful comments.

Supplementary Information for “A topological mechanism for robust and efficient global oscillations in biological networks”

Chongbin Zheng^{1,2} and Evelyn Tang^{1,2}

¹Department of Physics and Astronomy, Rice University, Houston, Texas 77005, USA

²Center for Theoretical Biological Physics, Rice University, Houston, Texas 77005, USA

I. ROBUSTNESS OF OSCILLATIONS IN OUR MODEL

In the topological regime ($\rho \gg 0$), our model supports global currents that propagate along the edge of the state space. The edge currents turn out to be robust against changes in the environment that render certain states inaccessible. For example, a limited number of KaiA molecules in solution could prevent the system from accessing the highly phosphorylated states, while a limited number of KaiB could block off hypophosphorylated states where x and y are small. Despite missing certain states in the lattice, the probability currents in our model can continue to propagate along the new edge of the state space, as illustrated by Fig. S1. The robustness in edge currents could explain how biological systems maintain stable dynamics in the face of changing external conditions.

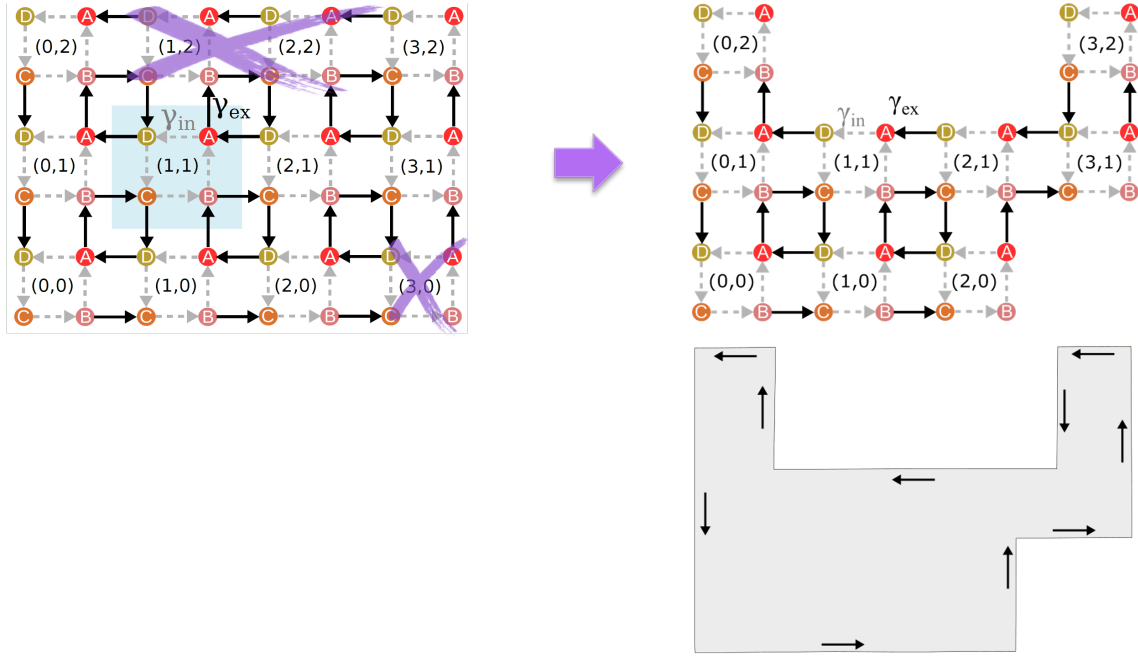


FIG. S1. **Topological protection ensures robustness of the edge state to obstacles or missing components.** In the presence of missing components or obstacles (purple crosses), the edge state (when $\gamma_{ex} \gg \gamma_{in}$) will simply go around them to maintain the largest available phase space. This robustness of the edge state can shed light on how biological systems can flexibly pivot in the presence of changing conditions or external stimuli. For illustration purposes, we use a smaller system with $N_x = 4, N_y = 3$ and only show the forward transitions γ_{ex} and γ_{in} .

The global oscillations in our model are also robust to perturbations in transition rates. The changes in rates can come from changing external conditions like concentrations of KaiA and KaiB or setting more biologically realistic transition rates for each reaction. They can also come from incorporation of additional KaiC reactions hitherto unconsidered. For instance, ATP association with the nucleotide binding site plays the same role as KaiA interaction in promoting T phosphorylation [1]. This reaction can be combined into the $S \rightarrow E$ internal transition, which results in an effective rate for the combined reaction that is larger than the rates for either reactions. To study the effects of such modifications, we make the rates non-uniform in different directions by multiplying each of $\gamma_{ex}, \gamma'_{ex}, \gamma_{in}, \gamma'_{in}$ in each direction (N,S,E,W) by a different random scaling factor f , taken from a normal distribution with mean 1 and standard deviation ϵ . We look at the real and imaginary spectral gaps and coherence of the resulting model, averaged

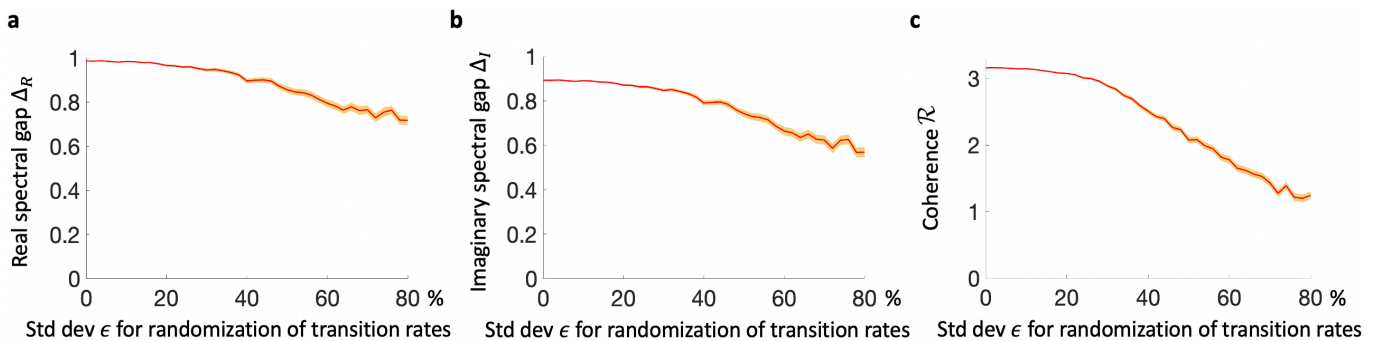


FIG. S2. **Spectral gaps and coherence for randomized transition rates.** **a**, Each transition rate ($\gamma_{ex}, \gamma'_{ex}, \gamma_{in}, \gamma'_{in}$) in the model is multiplied by a different random scaling factor f in each direction (N,S,E,W). f is taken from a normal distribution with mean 1 and standard deviation ϵ . In the case when a negative value is sampled, we take $f = 0$. Here we plot the real spectral gap Δ_R , averaged over different random realizations of transition rates, as a function of the standard deviation ϵ for randomization of the transition rates. The randomized rates repeat along the x and y axis. For example, any eastward γ_{ex} transition has the same rate after randomization regardless of the (x, y) coordinates. **b**, Average imaginary spectral gap Δ_I as a function of ϵ . **c**, Average coherence \mathcal{R} as a function of ϵ . For all panels, we average over 500 random configurations for each ϵ . The same configurations are used to calculate all three quantities. The yellow shaded area represent one standard error. The initial parameters for the model before multiplying by f are $\mu = 3, \rho = 5$.

over different random configurations of transition rates. As shown in Fig. S2, the spectral gaps do not close for ϵ up to 80%, so the network is still in the topological regime. In general, the steady state is still localized on the edge of the state space, even though it can have a higher probability in a particular edge, e.g., the left edge, because of the non-uniform transition rates. The coherence of the oscillation is attenuated but some degree of oscillation persists. The robustness of the oscillations obtain from its topological nature, and we expect it to remain robust, up to some extent, for other types of perturbations such as additions of long-range interactions that connect nonadjacent states in the state space.

II. THE 2D ZAK PHASE

Our model topology is characterized by the topological invariant known as the 2D Zak phase [2, 3]. It is defined as an integral over the 2D Brillouin zone:

$$\Phi_i^c = \frac{1}{2\pi} \int_{BZ} \mathbf{A}_i(k_x, k_y) dk_x dk_y, \quad (\text{S1})$$

where $\mathbf{A}_i(k_x, k_y)$ is the Berry connection for the i -th band, given by $\mathbf{A}_i(k_x, k_y) = i\langle\phi_i|\partial_{\mathbf{k}}|\psi_i\rangle$ for left and right eigenvectors $\langle\phi_i|$ and $|\psi_i\rangle$, respectively. For our stochastic system, we focus on the Zak phase Φ_h^c for the highest band h in real space (upper green band in Fig. 4b in the main text), which is the band closest to the steady state eigenvalue of 0. It turns out that when our system is in the trivial regime ($\rho < 0$), we have $\Phi_h^c = (0, 0)$. When our system is in the topological regime ($\rho > 0$), we have $\Phi_h^c = (\pi, \pi)$. The emergence of the dynamical regime with edge currents and edge-localized steady state coincides with a nontrivial 2D Zak phase, indicating its topological origin.

III. COHERENCE

In this section we motivate the definition of coherence in Eq. (2) in the main text and discuss why it can serve as a measure for the robustness of oscillations. We also discuss how coherence changes with the parameters μ and ρ .

For a master equation with non-degenerate eigenvalues

$$\frac{d\mathbf{p}}{dt} = \mathcal{W}\mathbf{p}, \quad (\text{S2})$$

the general solution is given by

$$p_i(t) = \sum_{\nu} c_{\nu} u_i^{\nu} e^{-\lambda_{\nu} t}, \quad (\text{S3})$$

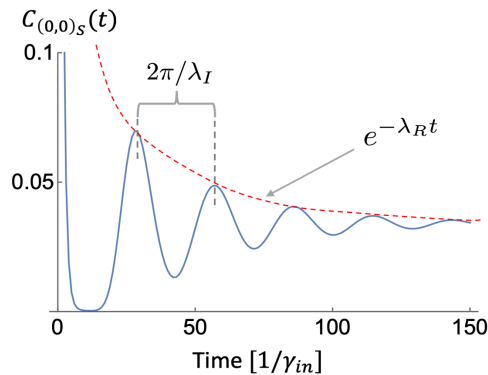


FIG. S3. **Correlation function $C_{(0,0)_S}(t)$ for the topological model goes through damped oscillations.** The oscillation has a decay time λ_R^{-1} and period $2\pi/\lambda_I$. Coherence is defined as the ratio between these two timescales, characterizing the number of coherent oscillations that can be maintained before approaching steady-state. Eventually, $C_{(0,0)_S}(t)$ approaches the steady-state probability p_i^s . Time is plotted in units of $1/\gamma_{in}$. The parameters used are $\mu = 7$, $\rho = 5$.

where λ_ν are the eigenvalues, $(u_1^\nu, u_2^\nu, \dots, u_n^\nu)^T$ are eigenvectors corresponding to λ_ν , and c_ν are constant coefficients that depend on initial conditions [4]. The eigenvalues λ_ν of the transition matrix \mathcal{W} characterizes the timescales of the probability evolution for the corresponding eigenmodes. If the network represented by \mathcal{W} is irreducible and ergodic, then there exists a unique steady-state distribution \mathbf{p}^s such that $\mathcal{W}\mathbf{p}^s = 0$, i.e., \mathbf{p}^s is an eigenvector of \mathcal{W} with a zero eigenvalue [4]. The dynamics of $\mathbf{p}(t)$, as we will see soon, is in general dominated by the first non-zero eigenvalue of \mathcal{W} , which is the eigenvalue with the smallest modulus in the real part [5]. Such eigenvalues generally come in conjugate pairs, denoted by $-\lambda_R \pm i\lambda_I$ for the real and imaginary parts λ_R, λ_I , respectively. In particular, we take $\lambda_R, \lambda_I \geq 0$ and $\lambda_1 = -\lambda_R + i\lambda_I$.

The dynamics of the system can be studied through correlation functions $C_i(t)$. Following [5], we define $C_i(t)$ to be the probability to find the system at state i at time t given that the system starts at state i at time $t = 0$, i.e., $C_i(t) = p_i(t)$ given the initial condition $p_i(0) = 1$ and $p_j(0) = 0$ for all $j \neq i$. Starting from a state on the edge, say, the lower left corner $(0,0)_S$, the correlation function $C_{(0,0)_S}(t)$ goes through damped oscillations (see Fig. S3). After some transient behavior in the first oscillation cycle, the dynamics is dominated by λ_1 , where the oscillation period is given by $T = 2\pi/\lambda_I$ and the exponentially decaying envelope has a decay time λ_R^{-1} [5]. Therefore, we follow [5] and define coherence as

$$\mathcal{R} \equiv \frac{\lambda_I}{\lambda_R}, \quad (\text{S4})$$

which, when divided by 2π , is the number of coherent oscillations that can be sustained before the system settles into the steady-state. The larger \mathcal{R} is, the more oscillations the system can maintain before stochastic fluctuations destroy its coherence.

In Fig. S4, we show a phase diagram for \mathcal{R} that include negative values of ρ (the trivial regime). \mathcal{R} turns out to be monotonic in both μ and ρ . \mathcal{R} increases monotonically in μ because a higher μ means a stronger external driving, making the forward reactions dominate more over their reverse reactions. This is more likely to give rise to trajectories with a particular chirality in our model. These trajectories correspond to the robust oscillations observed, and are less likely to backtrack or perform undirected diffusive motion when the external driving μ is large. For ρ , we can see that \mathcal{R} is always close to zero for $\rho < 0$. Large values of coherence is obtained only with positive ρ , even if the thermodynamic force μ is large. This is expected because $\rho \sim 0$ is the transition that separates the topological regime from the trivial regime. In the trivial regime, the system does not support an edge state, and the dynamics resembles random diffusion in the bulk rather than a directed motion along the boundary. Since there are no global oscillations in this regime, the coherence remains low. When ρ is positive and increasing, the system moves deeper into the topological regime, where the edge localization effects are more pronounced, leading to more robust oscillations.

IV. SINGLE-MOLECULE MODELS FOR KAIC

In this section, we include more details on the MWC model and the bilayer lattice model mentioned in the main text. Both models can be represented as directed networks and their dynamics described by corresponding master equations.

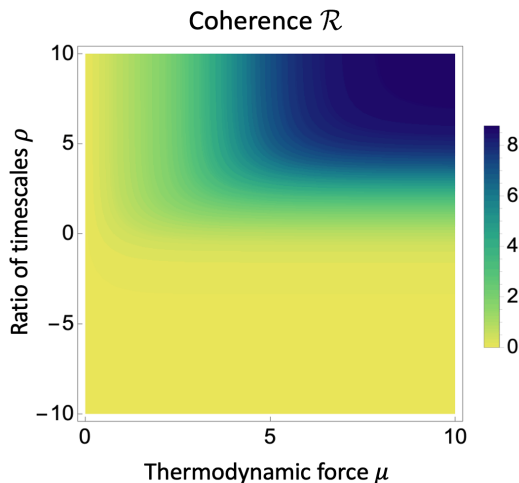


FIG. S4. **Phase diagram for coherence.** The range of ρ is extended from that of Fig. 3a to include negative values. \mathcal{R} is monotonic in both μ and ρ , and remain close to 0 in the trivial regime $\rho < 0$.

The MWC paradigm [6] was first applied to the KaiABC system by van Zon *et al.* [7], which assumed all-or-none conformational change for the entire KaiC hexamer. By assumption, the KaiC hexamer can only be in two conformational states, the active states C_i and the inactive states \tilde{C}_i , where the subscript $0 \leq i \leq 6$ represents the phosphorylation level of KaiC. There are 14 states in the state space in total. The network structure is shown in Fig. S5a.

In this paper we follow one of the simplest versions of MWC-type models described in [5] and use the same parametrization of the transition rates. When KaiC is in the active state, it is more likely to be phosphorylated. On the other hand, when KaiC is in the inactive state, it is more likely to be dephosphorylated. These dominant reactions are represented by the red vertical arrows in Fig. S5a with transition rates $\gamma e^{\eta/2}$. The reverse transitions (smaller black vertical arrows) have rates $\gamma e^{E/6}$. γ , η , and E are model parameters that can be varied. For the horizontal transitions in Fig. S5a, the rates from C_i to \tilde{C}_i are denoted as $k_{i\tilde{i}}$ and the rates from \tilde{C}_i to C_i are denoted as $k_{\tilde{i}i}$, where

$$k_{i\tilde{i}} = \begin{cases} 1, & i = 0, 1, 2, 3 \\ e^{E(i-3)/3}, & i = 4, 5, 6 \end{cases} \quad (\text{S5})$$

and

$$k_{\tilde{i}i} = \begin{cases} e^{E(3-i)/3}, & i = 0, 1, 2, 3 \\ 1, & i = 4, 5, 6 \end{cases}. \quad (\text{S6})$$

The value of γ sets the relative timescales between the phosphorylation/dephosphorylation reactions and conformational changes.

In Fig. S5b and S5c we show the network structure for the bilayer lattice model, adapted from Li *et al.* [8]. The state space consists of two layers of 7×7 lattices that are connected to each other. Fig. S5b shows the network structure of bottom layer from Fig. S5c. Similar to our topological model, the x and y coordinates (labeled by superscripts and subscripts C_y^x in Fig. S5b) represent T and S phosphorylation levels, respectively. The top layer has an identical structure to the bottom layer, with states labeled by \tilde{C}_y^x . C_y^x in the bottom layer corresponds to unbound KaiC while \tilde{C}_y^x in the top layer represents KaiB-bound KaiC. The system can make transitions $C_y^x \rightleftharpoons \tilde{C}_y^x$ between layers while keeping x and y coordinates fixed, which corresponds to KaiB binding and unbinding. To aid comparison, we simplify the model by parametrizing the transition rates with μ and ρ , the same parameters for our topological model. Within both layers, the orientations for faster reactions on each edge are chosen such that they form an overall counterclockwise cycle, to capture the order of the phosphorylation cycle (see Fig. S5b). These phosphorylation/dephosphorylation reactions (solid black arrows) are assumed to have uniform rates γ_{ex} while the slower reverse reactions have rates γ'_{ex} . On the other hand, the KaiB-binding transitions between layers have rates γ_{in} and γ'_{in} . In the upper right half of the lattice where the states are labeled green in Fig. S5b, the dominant reaction between layers is the upward KaiB binding transitions (green dashed arrows in Fig. S5c) with rates γ_{in} ,

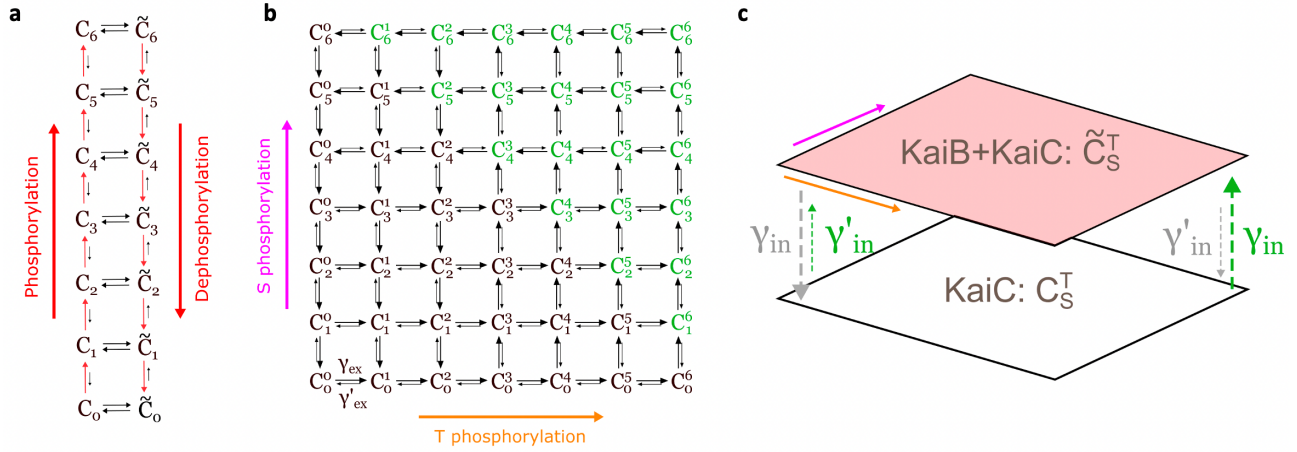


FIG. S5. **Single-molecule models for KaiC.** **a**, The MWC model. The KaiC hexamer can be in one of two conformational states, the active state C_i or the inactive state \tilde{C}_i . KaiC tends to phosphorylate in the active state and dephosphorylate in the inactive state, highlighted by the vertical red arrows. The slower reverse reactions are represented by smaller black vertical arrows. Horizontal transitions correspond to conformational changes of the KaiC hexamer between active and inactive states. **b**, The bottom layer of the bilayer lattice model. Subscripts x and superscripts y represent T and S phosphorylation level, respectively, just as for the topological model. Solid black arrows represent phosphorylation/dephosphorylation transitions with rates γ_{ex} and slower reverse rates γ'_{ex} . **c**, A zoomed-out view of the bilayer lattice model. Individual states in each layer are not shown. The green dashed arrows from the bottom to the top layer represent KaiB binding, while the gray dashed arrows from the top to the bottom layer represent KaiB unbinding. For the states colored green in **b**, transition rates are γ_{in} for KaiB binding and γ'_{in} for KaiB unbinding. For the states colored black, transition rates are γ'_{in} for KaiB binding and γ_{in} for KaiB unbinding. Larger dashed arrows (for any color) correspond to faster rates γ_{in} while smaller dashed arrows correspond to slower rates γ'_{in} . During KaiB binding and unbinding, the phosphorylation levels remain the same.

while the downward KaiB unbinding transitions (gray dashed arrows) have slower rates γ'_{in} . This is consistent with the fact that S phosphorylation promotes KaiB binding [9]. In the rest of the lattice where the states are labeled black in Fig. S5b, the dominant reaction between layers is the downward KaiB unbinding transition with rates γ_{in} , while the upward KaiB binding transitions take the slower rate γ'_{in} . This parametrization scheme gives rise to cycles where a KaiC molecule phosphorylates in the bottom layer, binds to KaiB, gets dephosphorylated in the top layer, and unbinds with KaiB to restart the cycle.

V. COST AND PRECISION FOR DIFFERENT KAIC MODELS

In this section we discuss how the free energy cost (quantified by ΔS) and the precision (quantified by \mathcal{R}) of various KaiC models change with the external driving μ . For the MWC model, the entropy production rate σ of the network can be obtained by a cycle decomposition method [4, 5]:

$$\sigma = \eta\gamma \sum_{i=0}^5 (e^{\eta/2} p_{C_i}^s - e^{E/6} p_{C_{i+1}}^s), \quad (\text{S7})$$

where $p_{C_i}^s$ is the steady-state probability at the state C_i . This expression is used to calculate the entropy production per period $\Delta S = \sigma T$ for the MWC model. As shown in the left column of Fig. S6, ΔS monotonically increases with \mathcal{R} , as expected. Coherence, however, is not monotonic in μ . When μ is sufficiently large, the MWC model ends up maintaining less coherent oscillations with increased driving and energetic cost. Note that the \mathcal{R} curve is different from the red dashed line shown in Fig. 3e in the main text. Here we plot \mathcal{R} with (η, E) held fixed, while the dashed line in Fig. 3e shows the maximum coherence for each μ for any parameter combinations (also see Methods). In contrast to the MWC model, coherence for the topological model increases monotonically in μ for a fixed ρ . ΔS , however, is non-monotonic, supporting a regime with increasing coherence and simultaneously decreasing cost (right column of Fig. S6). This unusual regime has its origin from the topological protection of the probability currents on the edge, which effectively reduces the state space into a one-dimensional cycle along the edge. This edge localization leads to a lower free energy cost but more coherent oscillations.

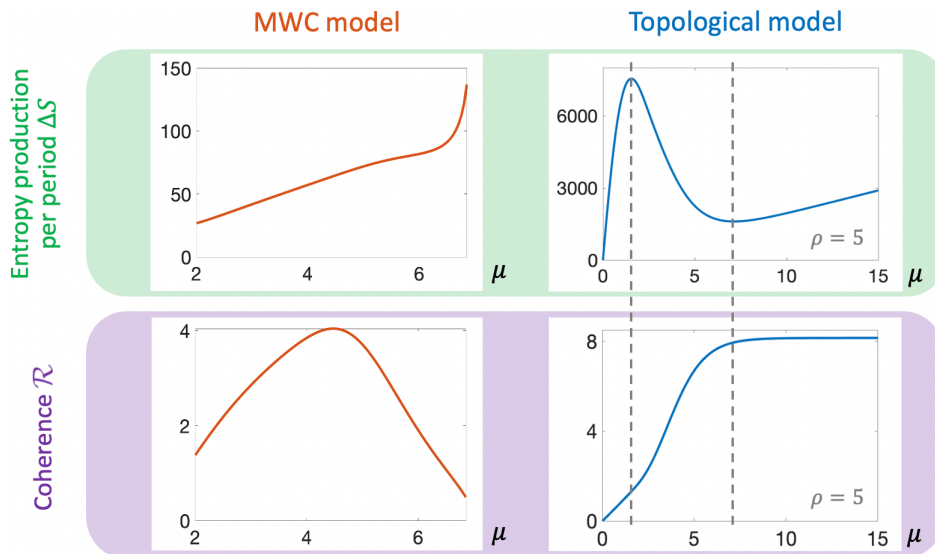


FIG. S6. **Entropy production per period and coherence for the MWC and the topological model.** The MWC model requires more entropy production to maintain a higher coherence, and its coherence decreases as still more entropy is produced under a stronger driving μ . On the other hand, the topological model supports a regime with increasing coherence but decreasing entropy production around $1.5 < \mu < 7$. For the MWC model, the parameters used are $\gamma = e^5$, $E = 10$. We plot μ in a smaller range for this model because outside the plotted range, we have $\lambda_I = 0$, which makes the oscillation period \mathcal{T} and hence entropy production per period ΔS ill-defined. Entropy production per period is given in units of $k_B \gamma_{tot}$.

VI. SPECTRAL GAP AS A PREDICTOR OF COHERENCE

In this section we study the effects of μ and ρ on the spectral gaps of the transition matrix \mathcal{W} with both periodic boundary conditions (PBC) and open boundary conditions (OBC), by tracking how the eigenvalues change with the two parameters. We also discuss why the spectral gap can serve as a predictor of coherence.

Spectral gaps can be defined for both PBC and OBC. Taking PBC, we can write the transition matrix in reciprocal space as

$$\mathcal{W}_{\mathbf{k}} = \begin{pmatrix} -\gamma_{tot} & \gamma_{in} + \gamma'_{ex} e^{-ik_y} & 0 & \gamma'_{in} + \gamma_{ex} e^{-ik_x} \\ \gamma'_{in} + \gamma_{ex} e^{ik_y} & -\gamma_{tot} & \gamma_{in} + \gamma'_{ex} e^{-ik_x} & 0 \\ 0 & \gamma'_{in} + \gamma_{ex} e^{ik_x} & -\gamma_{tot} & \gamma_{in} + \gamma'_{ex} e^{ik_y} \\ \gamma_{in} + \gamma'_{ex} e^{ik_x} & 0 & \gamma'_{in} + \gamma_{ex} e^{-ik_y} & -\gamma_{tot} \end{pmatrix}. \quad (\text{S8})$$

We obtain the spectral gaps for PBC from the continuous spectrum defined by $\mathcal{W}_{\mathbf{k}}$, as illustrated in Figs. 4a and 4b in the main text. Similarly, we can obtain spectral gaps for OBC by plotting the spectrum of \mathcal{W} in the complex plane, as in Fig. S7a. For each eigenstate ψ , we also calculate $\sum_{i \in \text{edge}} |\psi_i|^2$, the sum over the squared magnitudes

$|\psi_i|^2$ for all entries i that lie on the edge of the system. This quantity characterizes how localized the corresponding eigenstate is on the edge. We normalize each eigenstate so that the value of $\sum_{i \in \text{edge}} |\psi_i|^2$ can vary continuously between

0 and 1. A larger sum, or a redder color, indicates more edge localization. As we can see from Fig. S7a, the OBC spectrum displays two circle-like shapes with eigenstates highly localized on the edge and four clusters of eigenvalues, lying on the real or imaginary axis, with eigenstates more localized in the bulk. These four clusters are identified as the “bands” in the OBC case, in analogy with the four bands in the PBC spectrum as shown in Fig. 4a and 4b in the main text. As shown in Fig. S7a, we define the OBC real spectral gap Δ_R^o as the shortest distance from the leftmost band to the imaginary axis and the OBC imaginary spectral gap Δ_I^o as the shortest distance from the topmost band to the real axis.

In Fig. S7b we compare the imaginary spectral gap for PBC and OBC for the same parameters μ and ρ . The two gaps are almost identical at large ρ when the gap is large. When ρ is closer to 0, overlaps between the bands begin to develop for both PBC and OBC, which renders the spectral gap ill-defined. In the regime of relatively large ρ , spectral gaps for the OBC and PBC can be used interchangeably. The same conclusion can be drawn by looking at the two gaps with changing μ and fixed ρ . Therefore, to understand the relationship between coherence and the spectral gap, we can look at the OBC spectrum instead.

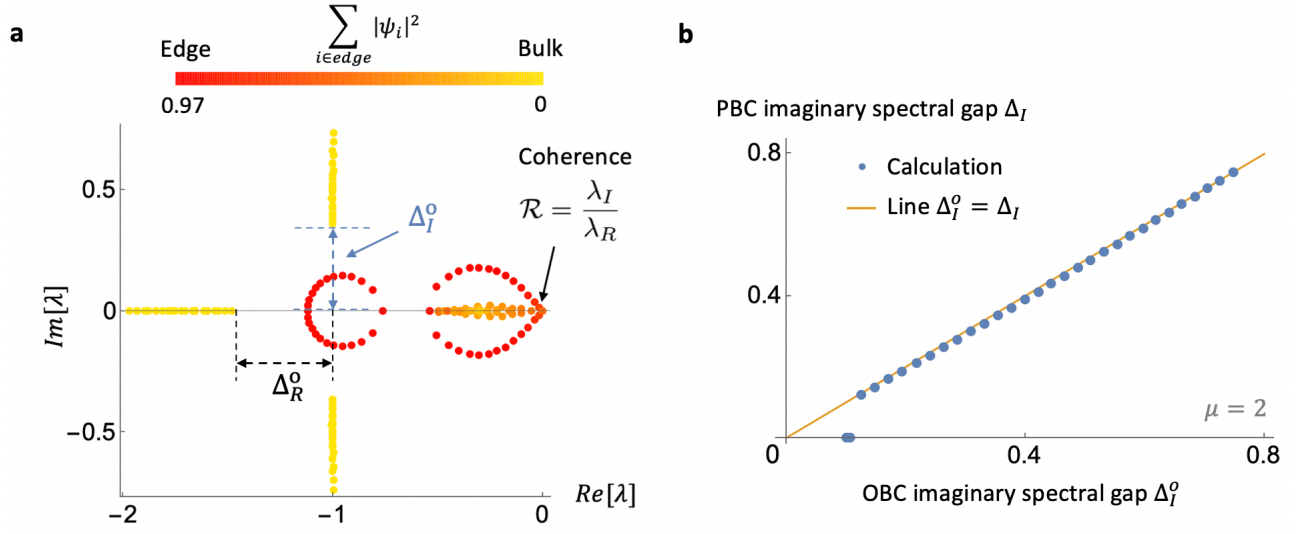


FIG. S7. **Spectral properties of \mathcal{W} in open boundary conditions (OBC).** **a**, Spectrum of \mathcal{W} in OBC. The real spectral gap is defined as the shortest distance between the left band to the imaginary axis, and the imaginary spectral gap is defined as the shortest distance between the top band to the real axis. The color for each dot corresponds to the value of $\sum_{i \in \text{edge}} |\psi_i|^2$, the sum of the magnitude squared of all entries in the steady-state eigenvector that lie on the edge. This quantity measures the extent to which the corresponding eigenvector is localized on the boundary of the system, and lies on a continuous spectrum between 0 and 1. A redder color means more localization. The solid black arrow points at the eigenvalue $\lambda_1 = -\lambda_R + i\lambda_I$, which determines the coherence \mathcal{R} . The parameters used are $\mu = 2, \rho = 1$. **b**, The imaginary spectral gaps defined in PBC and OBC are nearly identical when both gaps are large and the bands are well separated. ρ is varied from 0.2 to 4.6 in the plot while μ is fixed at $\mu = 2$. Calculated values for the two gaps (Δ_I in PBC and Δ_I^o in OBC blue dots) almost all lie on the orange line on which the two gaps are equal. Eigenvalues and spectral gaps are given in units of γ_{tot} .

Studying how λ_1 and the entire OBC spectrum change with μ and ρ gives a better picture of why coherence and the imaginary spectral gap track each other. Varying μ and ρ leads to global changes in the spectrum of \mathcal{W} in the complex plane, such as narrowing of the bandwidth or movement of all eigenvalues in a band in the same direction. Meanwhile λ_1 , the particular eigenvalue that determines coherence (see Fig. S7a), moves along with the bands in roughly the same way. When ρ is fixed, increasing μ has the effect of increasing the range or dispersion of the spectrum in the imaginary part. When $\mu = 0$, all reactions have symmetric rates with respect to their reverse reactions, and the system is in detailed balance. In this case, the spectrum is entirely real because \mathcal{W} is symmetric. Increasing μ therefore introduces nonzero imaginary parts to the eigenvalues, leading to oscillatory modes with faster timescales as the driving increases. For the top band, for instance, the imaginary parts of all eigenvalues in the band move upwards in the complex plane by roughly the same distance, keeping the bandwidth constant but increasing the distance between the bottom point in the band to the real axis (which is the definition of Δ_I^o). Meanwhile, the real parts of the eigenvalues in the four bands remain virtually unchanged with μ . As shown in Fig. S8a, λ_1 moves in a similar way with the global spectrum. Increasing μ leads to an increase in λ_I but very little change in λ_R . Since \mathcal{R} is proportional to λ_I while λ_R is roughly constant, coherence follows the same functional relationship as λ_I when μ increases (Fig. S8b). Therefore, since Δ_I closely tracks λ_I (see Fig. 4c in the main text), it also closely tracks \mathcal{R} monotonically.

On the other hand, ρ serves as an overall compression factor, decreasing the bandwidth for all four bands. The points farthest away from the real axis for the imaginary bands also increase slightly with ρ . The absolute values of these points equal the sum of the bandwidth for the imaginary band and the imaginary spectral gap. Therefore, a decrease in the bandwidth and an increase in the sum of the bandwidth and the spectral gap imply a monotonic increase in the spectral gap with increasing ρ . λ_1 in this case, however, does not always follow the general movement of the global spectrum. As shown in Fig. S8c, λ_R still decreases monotonically as expected, as the rightmost band is compressed toward the origin. λ_I , on the other hand, develops non-monotonic behavior. Nevertheless, when λ_I begins to decrease, it approaches zero more slowly than λ_R and gives rise to a monotonically increasing \mathcal{R} that tracks Δ_I^o (and therefore Δ_I) in ρ (Fig. S8d).

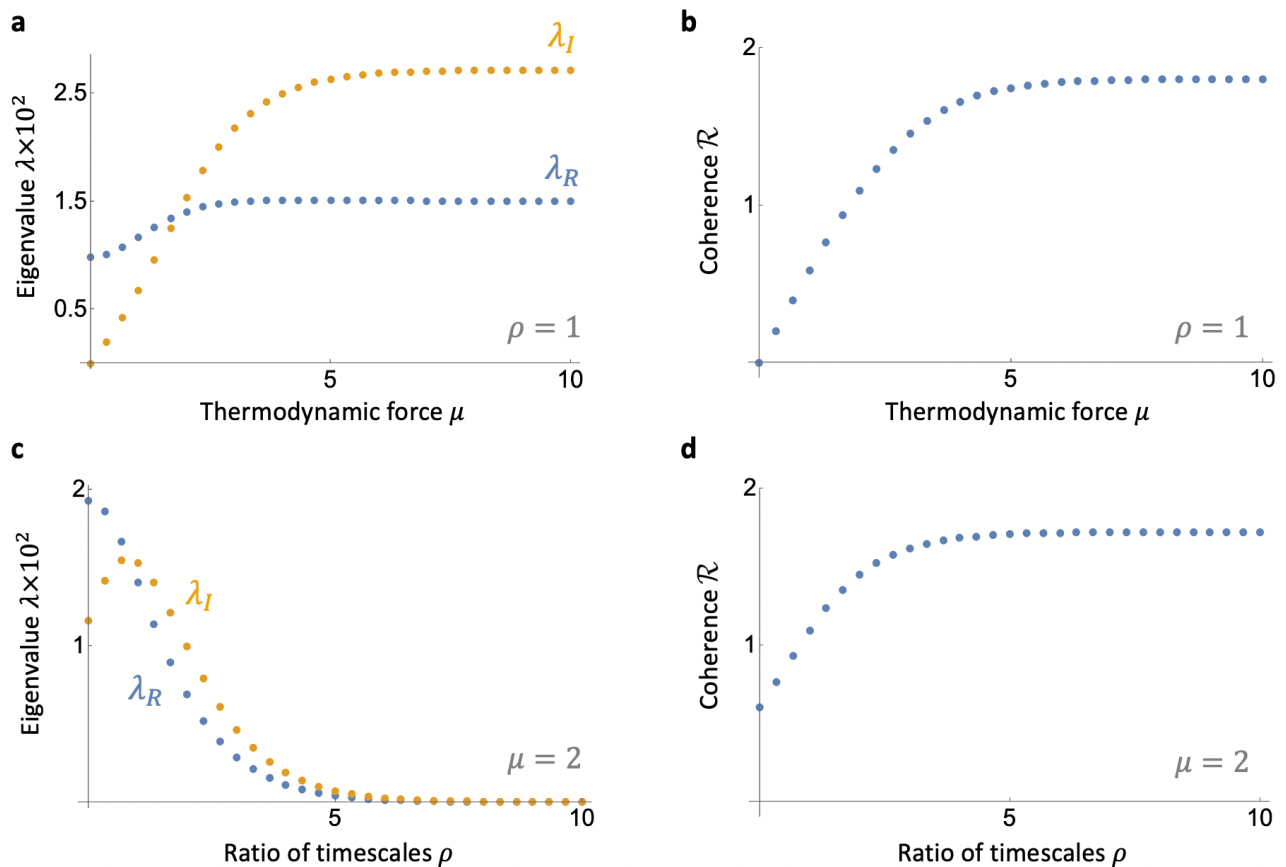


FIG. S8. **Effects of μ and ρ on the first non-zero eigenvalue λ_1 and coherence.** **a**, The absolute value of the real and imaginary parts for λ_1 as a function of μ . λ_I increases with μ and approaches a maximum while λ_R does not change significantly. **b**, Coherence as a function of μ . \mathcal{R} is almost proportional to λ_I given a nearly constant λ_R . **c**, The absolute value of the real and imaginary parts of λ_1 as a function of ρ . λ_R decreases monotonically while λ_I is non-monotonic in ρ . In the regime where λ_I decreases, it decreases slower than λ_R . **d**, Coherence as a function of ρ , showing a monotonic increase just as in the μ direction. Eigenvalues are given in units of γ_{tot} .

VII. GENERALIZATIONS TO MANY MOLECULES

In this section, we explore generalizations of our single-molecule model to many molecules. In particular, we investigate the higher-dimensional state space formed by two or more KaiC molecules. We further assume that KaiA is a scarce resource and study the resulting state space geometry modified by the constraints introduced by the competition over KaiA. This competition is intrinsically a population-level effect, as all KaiC molecules compete for the same scarce resource to complete the phosphorylation cycle. Finally, we look at the effects of limited or excess amounts of KaiA on the phosphorylation cycles for our single-molecule model or the many-molecule generalization.

We first look at the state space of our model when there are two KaiC molecules in consideration. In this case, the indices $(x_1, x_2, y_1, y_2)_{s_1, s_2}$ completely specify the system of two molecules, where the subscripts on the variables x, y, s denote molecule number. For each phosphorylation level (x_1, x_2, y_1, y_2) , there are $4 \times 4 = 16$ internal states that form a tesseract, the 4D generalization of a cube. These internal states repeat themselves in the four directions spanned by the external variables x_1, x_2, y_1, y_2 to form a state space in the shape of a 4D hypercube.

To study population-level effects, we assume that KaiA molecules, which promotes KaiC phosphorylation [10], are a scarce resource that can be depleted. This agrees with experimental observations that when KaiA concentrations drop below a certain point, oscillations are prohibited and KaiC phosphorylation levels remain low [11]. We further assume that each KaiA molecule promotes the T phosphorylation of one KaiC monomer. Since there are six T phosphorylation sites for each KaiC hexamer, we consider the regime $N_A < 12$, where the number of KaiA molecules N_A is not enough to fully phosphorylate both molecules. This competition introduces the constraint $x_1 + x_2 \leq N_A$. In the following, we consider the geometry of this state space in two cases. In either case, the hypercubic state space of the system is reduced to a hyperprism from the constraint introduced by competition over KaiA. Depending on

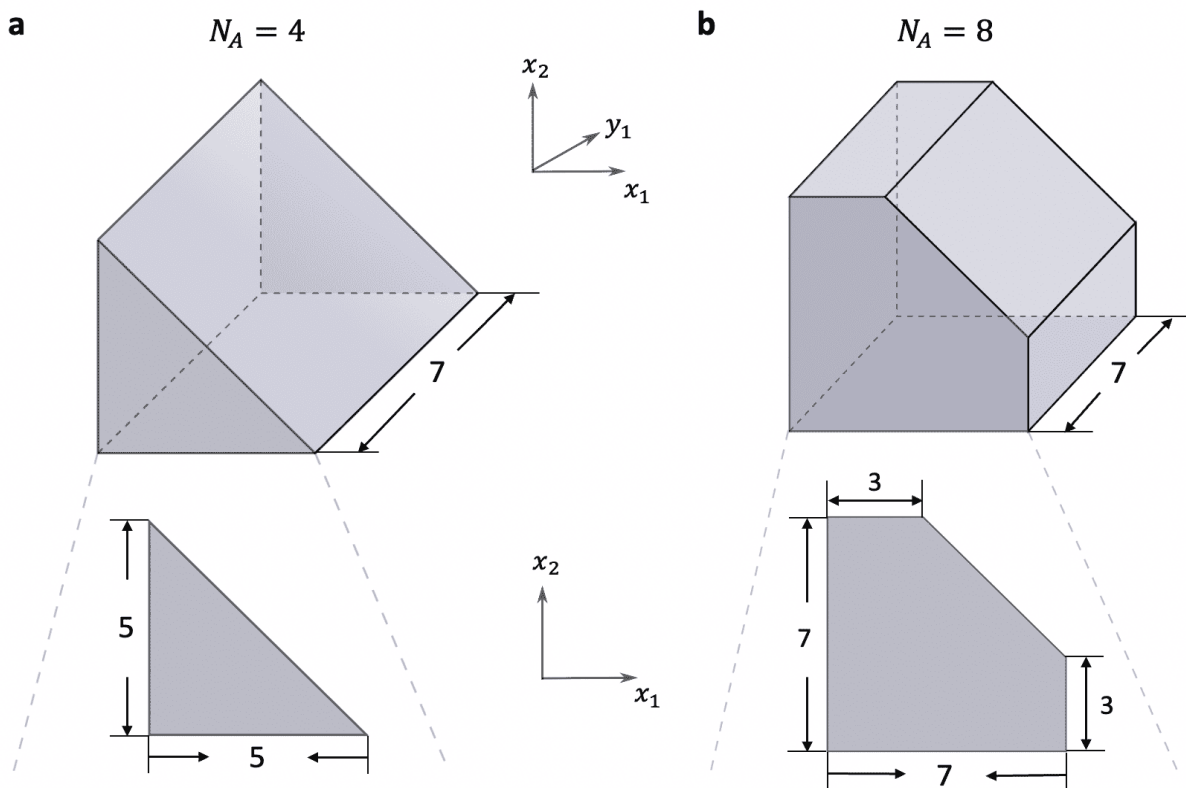


FIG. S9. Cross sections of the 4D state space for two KaiC molecules when competition for KaiA is taken into account. **a**, For $N_A = 4$, the constraint $x_1 + x_2 \leq N_A$ from competition over KaiA reduces the state space in x_1 - x_2 from a 7×7 square to an isosceles right triangle with side length 5. All side lengths refer to the number of phosphorylation levels contained in that direction. The 3D cross section in y_2 for the complete 4D state space is a right triangular prism, obtained by repeating the isosceles right triangle in y_1 . Such geometries come up in the regime $N_A \leq 6$. **b**, For $N_A = 8$, the constraint reduces the state space to an irregular pentagon in x_1 - x_2 , which results from cutting off a corner from a 7×7 square. The 3D cross section in y_2 is a pentagonal prism that derives from repeating the pentagon in y_1 . Such geometries come up in the regime $6 < N_A < 12$.

the amount of available KaiA, the cross-sections of the hyperprism can be different, as illustrated in Fig. S9. Such changes to the geometry of the state space modifies its edges and introduces dependence on phosphorylation levels of different molecules along these new edges, e.g., $x_1 + x_2 = 4$ on the hypotenuse of the triangle in Fig. S9a.

One regime is when $N_A \leq 6$. This is when KaiA can fully phosphorylate one KaiC hexamer at most. In this case, the x_1 - x_2 subspace will be reduced from a 2D square to an isosceles right triangle, as illustrated in the lower part of Fig. S9a, taking $N_A = 4$ as an example. To study the shape of the four-dimensional state space, we can look at its 3D cross-sections by holding one coordinate fixed. As shown in Fig. S9a, with a fixed y_2 , the state space in x_1 - x_2 - y_1 space is a right triangular prism, obtained by repeating the right triangle in x_1 - x_2 along the y_1 direction. This 3D cross-section is the same for any y_2 , which means that this prism repeats itself in the fourth dimension y_2 , forming a 4D hyperprism.

In another regime, $6 < N_A < 12$. This is when KaiA can fully phosphorylate one molecule but not enough to phosphorylate both. In Fig. S9b, we illustrate the geometry for the case $N_A = 8$. The x_1 - x_2 subspace is an irregular pentagon, formed by removing the upper right corner (an isosceles right triangle) from the 2D square. The 3D cross-section for a fixed y_2 is a pentagonal prism that repeats in y_2 to form another 4D hyperprism, which differs from the above by its different 3D cross-section.

In general, if there are N KaiC molecules, the constraint on the T phosphorylation levels becomes $x_1 + x_2 + \dots + x_N \leq N_A$. The state space will be a $2N$ -dimensional hyperprism, where high-dimensional “corners” are removed from a $2N$ -dimensional hypercube due to the constraint.

When the amount of KaiA is varied, this simple model behaves the same as what is observed in experiments, i.e., limited KaiA leads to sustained low levels of phosphorylation while excess KaiA leads to sustained high levels of phosphorylation [11, 12]. When there is little to no KaiA, states with high T phosphorylation levels are blocked.

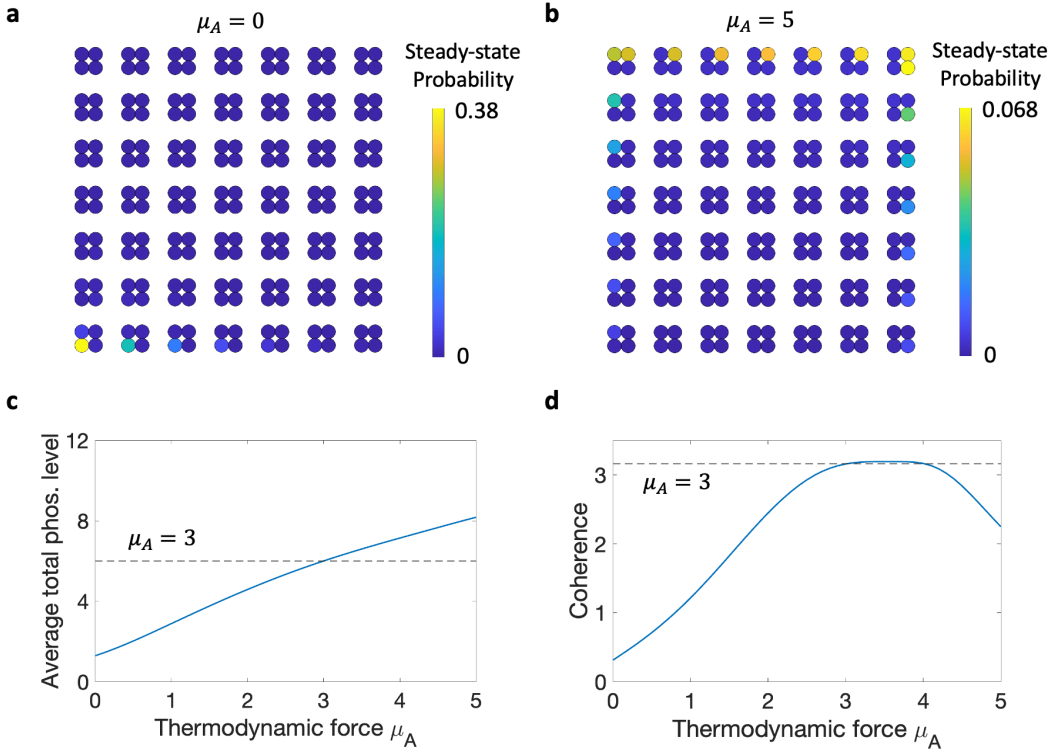


FIG. S10. **The effects of limited or excess amounts of KaiA on the KaiC phosphorylation cycle.** **a**, Steady-state probability distribution in the absence of KaiA. The thermodynamic force for the $S \rightarrow E$ internal transition, μ_A , which characterizes the external driving from interaction with KaiA, is set to be 0. The probability is localized on the lower left corner, corresponding to a hypophosphorylated state for KaiC in the absence of KaiA, consistent with experimental results [11]. In all panels, we take $\mu = 3, \rho = 5$. **b**, Steady-state probability distribution for $\mu_A = 5$. The probability is localized in highly phosphorylated states of KaiC, also consistent with experiments [12]. **c**, Total phosphorylation level of T and S as a function of μ_A , averaged over the steady-state probability distribution. KaiC autodephosphorylates as μ_A decreases with the removal of KaiA, and phosphorylates as μ_A increases with the addition of KaiA. $\mu_A = \mu = 3$ corresponds to the unmodified model as introduced in the main text, whose phosphorylation level is illustrated with a horizontal dashed line. **d**, Coherence as a function of μ_A . Coherent oscillations are inhibited with the removal of KaiA or an excess of KaiA. Coherence for $\mu_A = 3$ is illustrated with a horizontal dashed line.

When there is too much KaiA, there is no competition and no constraint whatsoever on the state space, which means that each KaiC molecule oscillates independently without synchronizing. Moreover, the strong driving from KaiA would promote phosphorylation of each molecule (see Fig. S10b), leading to a high overall phosphorylation level. We note that the above discussions have relied on simplifying assumptions on the nature of KaiA-KaiC interactions. A more thorough investigation of a many-molecule model would take into account more realistic properties of KaiA.

Such effects of KaiA can also be captured just by our single-molecule model in the main text. Because the thermodynamic force for the $S \rightarrow E$ internal transition, which we denote as μ_A , characterizes the driving from interaction with KaiA, changes in μ_A correspond to changes in concentrations of KaiA [13]. We keep the slower $E \rightarrow S$ transition rate fixed at γ'_{in} and let the $S \rightarrow E$ transition rate depend on μ_A by $\gamma'_{in} e^{\mu_A/k_B T}$. Fig. S10a shows the steady-state probability distribution for $\mu_A = 0$ while μ and ρ are kept the same, which corresponds to complete removal of KaiA. As we can see, the probability is mostly localized in states near the lower left corner, corresponding to low levels of phosphorylation. In contrast, in Fig. S10b we set $\mu_A = 5$, corresponding to excess amounts of KaiA. The probability, in turn, becomes localized in highly phosphorylated states. The average total phosphorylation level (T and S combined) as a function of μ_A is shown in Fig. S10c, which shows increasing levels of phosphorylation as μ_A increases and KaiA is added. For either limited ($\mu_A < 3$) or excess ($\mu_A > 3$) amounts of KaiA, oscillation tends

to be attenuated as illustrated by the decrease in coherence in Fig. S10d.

-
- [1] T. Nishiwaki and T. Kondo, Circadian autodephosphorylation of cyanobacterial clock protein KaiC occurs via formation of ATP as intermediate, *Journal of Biological Chemistry* **287**, 18030 (2012).
 - [2] F. Liu and K. Wakabayashi, Novel topological phase with a zero berry curvature, *Physical review letters* **118**, 076803 (2017).
 - [3] E. Tang, J. Agudo-Canalejo, and R. Golestanian, Topology protects chiral edge currents in stochastic systems, *Physical Review X* **11**, 031015 (2021).
 - [4] J. Schnakenberg, Network theory of microscopic and macroscopic behavior of master equation systems, *Reviews of Modern physics* **48**, 571 (1976).
 - [5] A. C. Barato and U. Seifert, Coherence of biochemical oscillations is bounded by driving force and network topology, *Physical Review E* **95**, 062409 (2017).
 - [6] J. Monod, J. Wyman, and J.-P. Changeux, On the nature of allosteric transitions: a plausible model, *Journal of molecular biology* **12**, 88 (1965).
 - [7] J. S. van Zon, D. K. Lubensky, P. R. Altena, and P. R. ten Wolde, An allosteric model of circadian KaiC phosphorylation, *Proceedings of the National Academy of Sciences* **104**, 7420 (2007).
 - [8] C. Li, X. Chen, P. Wang, and W. Wang, Circadian KaiC phosphorylation: a multi-layer network, *PLoS computational biology* **5**, e1000568 (2009).
 - [9] G. K. Chow, A. G. Chavan, J. Heisler, Y.-G. Chang, N. Zhang, A. LiWang, and R. D. Britt, A night-time edge site intermediate in the cyanobacterial circadian clock identified by EPR spectroscopy, *Journal of the American Chemical Society* **144**, 184 (2022).
 - [10] Y. Xu, T. Mori, and C. H. Johnson, Cyanobacterial circadian clockwork: roles of KaiA, KaiB and the kaiBC promoter in regulating KaiC, *The EMBO Journal* **22**, 2117 (2003).
 - [11] H. Kageyama, T. Nishiwaki, M. Nakajima, H. Iwasaki, T. Oyama, and T. Kondo, Cyanobacterial circadian pacemaker: Kai protein complex dynamics in the KaiC phosphorylation cycle in vitro, *Molecular cell* **23**, 161 (2006).
 - [12] A. G. Chavan, J. A. Swan, J. Heisler, C. Sancar, D. C. Ernst, M. Fang, J. G. Palacios, R. K. Spangler, C. R. Bagshaw, S. Tripathi, *et al.*, Reconstitution of an intact clock reveals mechanisms of circadian timekeeping, *Science* **374**, eabd4453 (2021).
 - [13] T. L. Hill, *Free energy transduction and biochemical cycle kinetics* (Springer-Verlag New York Inc., 1989).